This is a non-peer-reviewed pre-print submitted to EarthArxiv

Rift-Induced Repositioning of Mantle Plumes Beneath the Indian Lithosphere: Implications for Deccan Volcanism

Dip Ghosh[1], Joyjeet Sen[2], Nibir Mandal[2*]
[1]Department of Geology, University of Calcutta, Kolkata 700019
[2]Department of Geological Sciences, Jadavpur University, Kolkata 700032
Corresponding author: nibir.mandal@jadavpuruniversity.in

Abstract

Indian craton comprises a number of old rifts, e.g., the Narmada, the Mahanadi and the Godavari rifts, which reactivated in multiple stages during the supercontinent breakup events. The latest reactivation of the Indian rift system occurred at the Cretaceous-Tertiary boundary when the Réunion plume interacted with the Indian plate, leading to the massive Deccan volcanism at 66 Ma. Although the plume-driven rift tectonics has been a subject of lively research over past decades, how a pre-existing rift system can modulate the plume dynamics, particularly in continental settings, remains inadequately explored. This study addresses this problem in the context of the Réunion plume encountering the Indian lithosphere. We develop 2D thermomechanical models to simulate plume-rift interactions, systematically investigating the modes of interactions as a function of plate velocity (V_p) and plume–rift (δ) distance. Our numerical experiments reveal that small δ (< 250 km) or high V_p (> 1cm/year) conditions redirect a large portion of the plume material towards the pre-existing rift, resulting in significant underplating and subsequent melting beneath the rift undergoing reactivation. Increasing δ or lowering of V_p weakens the plume-rift interaction, leaving the pre-existing rift zone almost passive, where the underplated plume materials stagnate beneath the lithosphere with little melting. The model results suggest that the Narmada rift, which was closer to the Réunion plume, caused significant deflection of the plume and its melting with Moho upwraping. In contrast, the Godavari rift, located at a larger distance from the plume, behaved passively, allowing underplating of the plume at the lithospheric base with no significant melting and Moho downwraping, as supported by geophysical observations. Finally, this study provides a new insight into the differential responses of the Indian rift system during the Reunion plume event.

1. Introduction

Continental rifts often exhibit spatiotemporal correlations with large igneous provinces (LIPs), such as the Deccan Trap in peninsular India, which generally cover vast areas of the continental surface, exceeding 1 million km² (Bryan and Ferrari, 2013; Ernst, 2014). Although the precise geodynamic relationship between flood basalt eruptions in LIPs and continental rifting remains uncertain, it is now well-established that these two large-scale processes, rifting and plume-driven LIP volcanism, interact in complex ways, leaving intertwined signatures in the geological record. Seismic tomographic studies (French and Romanowicz, 2015) often reveal a close spatial association between mantle plumes and continental rift events during specific periods in their geological evolution. This connection is supported by geophysical and geochemical anomalies observed along rift zones, such as positive Bouguer anomalies, increased seismic wave velocities, and elevated Moho depths (Funck et al., 2007; Kendall et al., 2006). Several authors argue that mantle plumes play a significant role in modulating rifting events, either by facilitating the migration of rift centers or causing their complete cessation, depending on the relative positions of the plume and the rift (Mittelstaedt et al., 2011; Whittaker et al., 2015). Understanding the mechanisms of plume–rift interaction has thus become a challenging and critical area of research since the early 1980s (Morgan, 1978), particularly to explain the widespread volcanism observed in continental regions (Koppers et al., 2021; Richards et al., 1989; White and McKenzie, 1995). In parallel, studies of mid-ocean ridge systems representing divergent oceanic plate boundaries have identified several key factors that govern plume–ridge interactions. These include seafloor spreading rates, plume buoyancy flux, and the spatial distance between the plume and the ridge (Ito et al., 2003; Kinchid et al., 1995; Mittelstaedt et al., 2011; Pang et al., 2023; Ribe, 1996; Ribe and Christensen, 1994; Sleep, 1997). Additionally, the trench-ward viscous drag of plates and rift-ward pressure-induced forces have been recognized as influential parameters (François et al., 2018).

Laboratory experiments and numerical simulations have provided significant insights into the thermo-mechanical effects of plume–lithosphere interactions during rift evolution (Ribe and Christensen, 1994). Lithospheric heating caused by mantle upwelling and associated magma emplacement leads to mechanical weakening, which can greatly facilitate the rifting process (François et al., 2018). In turn, rifting enhances the extraction of melts generated by decompression melting in the asthenosphere. Divergent mantle flows beneath rift zones create regions of low dynamic pressure, which draw plume material toward the rift axis (Ribe and

Christensen, 1994; Sleep, 1997). However, this ascent becomes more complex due to additional forces exerted by tectonic plate movements, which can pull plume material away from the axial zones of rift systems (Ribe and Christensen, 1999, 1994). These competing forces, gravitational and tectonic, play critical roles in modulating plume–rift interactions, yet their relative contributions remain poorly quantified. The plume-induced rifting model has successfully explained key features of many active and ancient rift systems, such as the volcanic patterns and basin formation observed in the East African Rift System (Issachar et al., 2024). Nevertheless, several aspects of plume-associated lithospheric phenomena remain unresolved. For instance, the mechanisms governing the distribution of hotspots, particularly rift-ward spreading versus plate-drag spreading, are not yet fully understood. Addressing these gaps is essential for a more comprehensive understanding of the dynamic interplay between mantle plumes, lithospheric deformation, and tectonic processes.

Previous studies, as discussed earlier, have primarily focused on the mechanical and thermo-mechanical effects of mantle plumes on the overlying lithosphere, particularly in the context of interpreting continental rift tectonics (Burov & Gerya, 2014; Burov & Guillou-Frottier, 2005; Gibson et al., 1999; Kendall et al., 2005; Larsen & Saunders, 1998; Sleep, 1997). However, many continents host rift systems that predate specific plume events. Geological evidence indicates that these pre-existing rifts can significantly influence the ascent dynamics of mantle plumes, resulting in a strong spatiotemporal correlation between plume-associated magmatism and rift zones (Issachar et al., 2024). The mechanisms by which a pre-existing rift redirects a plume upon its encounter with the lithosphere, however, remain relatively underexplored. Recent model simulations by Pang et al. (2023) demonstrate that divergent mid-ocean ridges can strongly interact with off-axis plumes, redirecting plume material flow either toward or away from the ridge axis. This redirection depends on the interplay between plate drag and the gravitational force driving plume flow along the base of the sloping lithosphere. Their findings suggest that strong buoyant mantle plumes tend to flow toward the ridge axis under slow spreading conditions and small plume- ridge distances. Conversely, under fast spreading conditions and in the presence of smaller or intermediate plumes with larger plume–ridge distances, the flow is directed away from the ridge. While these results provide valuable insights into oceanic settings, further investigation is needed to understand the dynamics in continental environments. Specifically, the role of pre-existing rifts in modulating plume stagnation and remobilization beneath the lithosphere of mechanically strong continental plates remains an open question. Advancing this understanding is essential for elucidating the interactions between mantle plumes and continental lithosphere in tectonic and magmatic processes.

To investigate this issue in a continental geodynamic context, we focus on the geological settings of the closely associated Deccan Volcanic Province (DVP) and major rift systems in peninsular India (Fig. 1a). This rifted region experienced a remarkable volcanic event that produced extensive flood basalts exceeding 1.5 km in thickness and covering over 500,000 km^2. The DVP is genetically linked to the Reunion hotspot, which the northward-drifting Indian plate encountered around 66 Ma (Sprain et al., 2018). Geological evidence suggests that pre-existing rifts in the Indian continent significantly influenced plume-driven magmatic emplacement. One such rift is the Cambay Rift (CBR), which divides the Deccan Traps into two distinct units: north-west and south-west (Rao et al., 2015). The Cambay Rift, filled with Tertiary sediments, is interpreted as a failed rift formed by extensional tectonics. Other major rift systems in the Indian peninsula include the Godavari Graben (GG) and the Mahanadi Rift (MHR). Although these are passive features, they have left distinct surface imprints. Studies indicate that the GG has redirected magma pathways (Keller et al., 2008), citing as a potential zone for accumulating plume material. Another prominent tectonic feature is the Narmada-Son Lineament (NSL), an approximately east-west structure originating in the Archean era. The NSL divides various tectonic zones in northern and southern India (Kumar et al., 2015). All these paleo-rifts have existed since the Precambrian era within the Indian craton (Fig. 1b) and are believed to have acted as zones of weakness during major geological events (Meert et al., 2010; Patranabis-Deb et al., 2020). Despite their potential importance, the influence of these pre-existing weak zones on the DVP—India's most remarkable volcanic event—remains largely unexplored. Understanding their role could provide valuable insights into the interaction between mantle plumes and lithospheric structures in shaping this geologic phenomenon, which sets the principal motivation of our present study.

We developed a thermo-mechanical geodynamic model to explore the influence of the Réunion plume on the reactivation of pre-existing rift zones within the Indian craton. Additionally, the model examines the feedback effects of this rift reactivation on the plume's repositioning during its interaction with the overlying lithosphere. This study reveals how the major rift systems in the Indian peninsula regulated the distribution of plume materials beneath the continental lithosphere during the Deccan volcanic event in the Cretaceous period. The article also highlights the striking differences between the eastern and western rift systems and their respective interactions with plumes. The article is organized as follows: the first section presents a comprehensive historical overview of two major Phanerozoic events—continental rifting and plume-driven Deccan volcanism—highlighting their spatial and temporal correlations. The second section outlines the modeling approach employed to study the mode of plume–rift interactions in a continental setting. Subsequently, the model results are presented, illustrating how rifting influences the repositioning of plumes during their interaction with the lithosphere as functions of various physical parameters, including plume size, ridge spreading rate, plume–rift distance, and lithospheric strength. The article finally discusses the interactions between major old Indian rifts and the Reunion plume in light of the model findings.

2. Continental rifts and Deccan volcanism

2.1. Rift tectonic history

The Indian rift system primarily comprises four major rifts: the Narmada-Tapti rift in central India, the Mahanadi and Godavari rifts in the Indian Peninsula, and the Cambay rift along the western margin (Fig. 1a). The rift-controlled Narmada-Son valley region is thought to have originated during the Archean era and has been reactivated multiple times throughout subsequent geological events (Fig. 1b) (Choubey, 1971; Kumar et al., 2015; Naveen et al., 2023). The Narmada-Tapti (NT) rift broadly follows E-W to ENE-WSW trending lineaments, marking a significant tectonic boundary between the southern Peninsular region and the northern foreland. These Precambrian lineaments, often referred to as lithospheric weak zones or paleo-rifts, appear to have played a critical role in the NT rift formation, with mafic intrusions aligning along these structural features. Similarly, the western continental margin exhibits numerous N-S to NNW-SSE oriented lineaments that facilitated rifting and the subsequent breakup of the Indian craton. Geochronological studies indicate that the Narmada-Son Lineament (NSL) formed during the Neoarchean to Neoproterozoic eras, experiencing multiple tectonic events between 2.2 and 0.9 Ga (Fig. 1b). Some researchers suggest that the Mahakoshal group of rocks, located between the Son-Narmada Northern Fault (SNNF) and the Son-Narmada Southern Fault (SNSF), represents a back-arc rift environment associated with Paleo-Proterozoic subduction (~1.8 Ga) (Bhowmik et al., 2012; Chattopadhyay et al., 2020). This active subduction culminated during the Meso-Proterozoic (~1.5 Ga), resulting in a continent–continent collision.

The Mahanadi and Godavari rifts are considered extensions of the Central Indian Tectonic Zone (CITZ) to the eastern margin of India, thought to have originated during the breakup of the supercontinent Columbia between 1.7 and 1.5 Ga (Fig. 1b). Plate reconstructions suggest that the Gondwanaland comprised several major cratons that amalgamated through continental collision tectonics by the end of the Proterozoic, maintaining this assembly until the Jurassic or Early Cretaceous periods. During the Cambrian period, East Gondwana comprised India, Madagascar, Western and Northern Australia, and East Antarctica, while West Gondwana comprised Africa and South America. These two parts developed a suture zone along a Neo-Proterozoic mobile belt (Ghosh, 2015; Unrug, 1996). In the Carboniferous period (330–320 Ma), the Gondwanaland collided with North America, Europe, and Siberia to form the supercontinent Pangea. Pangea remained intact until the Jurassic period, when it began to fragment due to successive rifting events. The breakup commenced with the separation of North America from Africa–South America, marked by the opening of the Central Atlantic Ocean around 195 Ma. This event is associated with extensive volcanism that created the vast (>1 million km^2) Central Atlantic Magmatic Province (CAMP) at approximately 201 Ma (Mchone, 2000), which is generally linked with the Triassic–Jurassic mass extinction event (Blackburn et al., 2013; Marzoli et al., 1999). Geological records indicate that these tectonic activities reactivated the eastern margin rifts, including the Mahanadi and Godavari rifts and the eastern part of the CITZ.

The Narmada-Tapti rift was reactivated later, during the Jurassic period (~175 Ma) (Fig. 1b), when the western half of Gondwana (Africa and South America) began to separate from the eastern half (India, Madagascar, Australia, and Antarctica). Around 140 Ma, Africa and South America split, forming the South Atlantic Ocean. On the other hand, the separation of India and Madagascar from Antarctica and Australia formed the central Indian Ocean. This process is associated with the eruption of the Rajmahal Traps (115–118 Ma) in eastern India at (Baksi, 1995) and the Bunbury Traps (132 Ma) in Western Australia (Torsvik and Cocks, 2013). India finally broke away from Madagascar during the Late Cretaceous, accompanied by the eruption of the Deccan flood basalts. This massive volcanism occurred between 67 and 65 Ma (Chenet et al., 2007, spreadingest to east along preexisting structural weaknesses in the CITZ (Bhattacharji et al., 1996). This event also led to the formation of the Cambay rift (Rao et al., 2015). The extensive Deccan volcanism occurred in three distinct phases, resulting in the formation of a primary magmatic chamber at the crust-mantle boundary as an underplated layer (Ju et al., 2013) and a secondary magma chamber at shallow crustal levels (Bhattacharji et al.,

1996) in the Narmada-Tapti region. The central portion of the CITZ and surrounding Mesozoic sediments are predominantly buried beneath Deccan flood basalts, which obscure the subsurface structure and pre-volcanic tectonics of the Narmada-Tapti zone. The primary landform of this rift valley is the Cretaceous peneplain, which was rifted and subsequently buried by extensive lava flows.

2.2. Geodynamics of the Deccan volcanism

The Deccan Volcanic Province (DVP) is stratigraphically divided into three principal subgroups based on volcanological and geochemical characteristics: the Kalsubai, Lonavala, and Wai subgroups. The Cretaceous–Paleogene boundary (KPB), dated to 66.043 ± 0.043 Ma (Sprain et al., 2018), falls within the Khandala, Bushe, or Poladpur Formations, approximately 165 ± 68 ka after the emplacement of the Kalsubai subgroup. Recent geochronological studies of the Deccan Traps (DTs), utilizing $^{40}Ar/^{39}Ar$ dating of plagioclase from basalt flows and U-Pb dating of zircon from ash-bearing intervals (Keller et al., 2012; Richards et al., 2015; Schoene et al., 2019, 2015), have constrained the sequence of eruption events. These investigations converge to the point that the main eruptive phases began shortly before the C30n-C29r geomagnetic reversal and ended after the C29r-C29n reversal. The formations above the KPB, belonging to the Wai subgroup, are distinct in their geochemistry and volcanological features, such as voluminous eruptions and greater susceptibility to weathering. Using $^{40}Ar/^{39}Ar$ geochronology, earlier studies identified four to five distinct eruption events at approximately 62.5, 63.7, 65.6, 66.6, 67.8, and 69.7 Ma (Chenet et al., 2007), suggesting time intervals of ~1–1.9 Ma between successive events. Similarly, Parsio et al. (2016) recognized five eruption peaks at 64.1, 65.2, 66.2, 67.5, and 69.6 Ma, with intervals ranging from ~1.1–2.1 Ma. More recent investigations utilizing high-precision U-Pb geochronology (Schoene et al., 2019)), have identified three to four discrete pulses during the main eruption phase near the KPB, each lasting less than 100 ka. These pulses include- First Pulse: Eruption of the lowermost seven formations (~66.3 - 66.15 Ma); Second Pulse: Emplacement of the Poladpur Formation (~66.1 - 66.0 Ma); Third Pulse: Formation of the Ambenali Formation (~65.9 - 65.8 Ma); Fourth and Final Pulse: Eruption of the uppermost Mahabaleshwar Formation (~65.6 - 65.5 Ma).

Recent studies have correlated the Deccan volcanic event with Réunion hotspot activities, explaining the underlying geodynamic processes in connection with the African Large Low Shear Velocity Province (LLSVP) (Ghosh et al., 2024). Glišović and Forte (2017) integrated data from the Deccan Continental Flood Basalts (CFB), the Réunion Ocean Island Basalts (OIB), and other similar hotspot tracks from a geophysical perspective and proposed a mantle plume hypothesis as the origin of the Deccan Large Igneous Province (LIP). The coeval relationship between Deccan volcanism and the plume-induced rapid acceleration of the Indian plate during the Cenozoic to late Cenozoic also supports this hypothesis. Interestingly, as with other hotspots, such as Iceland and Tristan da Cunha, the Réunion hotspot is located at the edge of the African LLSVP, suggesting that the LLSVP may have acted as a primary feeder for the plume, at least during the Cenozoic (Petersen et al., 2016; Zhao, 2015). Recent isotopic (Sr-Nd-Os) studies of primary magmas from Réunion provide geochemical evidence for a temporally stable mantle plume, with its primary reservoir linked to the African LLSVP. Furthermore, recent geodynamic models indicate that plume activity occurred episodically, controlled by its interactions with the 660-km transition zone (Ghosh et al., 2024).

The pre-existing continental rifts significantly influenced the pathways of plume materials and the massive eruption of Deccan basalts across the Indian craton. Some studies have shown that the eruption began along east-west trending pre-existing weak zones within the Central Indian Tectonic Zone (CITZ) (Bhattacharji et al., 1996). During the first phase of the eruption, the Réunion hotspot was positioned at the lithospheric base beneath the Nasik–Pune region. In the second phase, this position shifted to a new location beneath the west coast (Chenet et al., 2007; Ju et al., 2013). Additionally, Deccan Trap (DT) rocks have been reported from the Rajahmundry region, south of the Godavari Rift, suggesting that the plume activity reactivated the rift and facilitated magma eruptions through faults in the reactivated zone (Singh et al., 2012). Crustal velocity structures indicate significant magmatic underplating, extending from the western flank to the middle and eastern segments of the Narmada–Son Lineament (NSL) (Kaila et al., 1987; Singh, 1998). Geophysical observations show that the average crustal thickness near the NSL is approximately 40 km, deepening to ~55 km within the lineament zone. High Vp/Vs ratios (1.84) in the thicker crustal regions suggest an accumulation of mafic to ultramafic materials in the lower crust (Kumar et al., 2015; Rai et al., 2005). Similarly, in the Mahanadi Rift region, active seismic refraction studies have identified a high-density (3.05 g/cm^3) layer at the base of the crust (Behera et al., 2004). Researchers propose that these observations can be explained by Moho upwarping or crustal thinning in the rift zone, accompanied by the emplacement of thick, high-velocity materials. It has been hypothesized that the basaltic underplating in these regions may have originated from Kerguelen hotspot activity, which is also believed to be responsible for the ~130 Ma Rajmahal

Traps in eastern India (Curray and Munasinghe, 1991; Krishna et al., 2012; Olierook et al., 2019). The complex nature of the Moho beneath the NSL and other basins, such as the Mahanadi and Godavari basins, is thus often attributed to magmatic underplating associated with rift environments. This magmatic underplating within the crust likely reflects lithospheric stretching and reactivation of the rift system.

3. Thermo-mechanical modelling

3.1 Approach

The models are constructed using 2D Cartesian geometry, encompassing a horizontal distance of 1000 km and a vertical extent of 440 km. The vertical domain is divided into seven horizontal compositional layers. The uppermost layer, which represents sticky air, has a thickness of 30 km. Beneath this, the crustal layer is divided into two sub-layers: the upper crust, 25 km thick, and the lower crust, 15 km thick. Below the crust, the mantle lithosphere has a thickness ranging from 40 to 80 km. The remaining portion of the model domain represents the upper mantle. To simulate plumes in the thermomechanical model, a semicircular material domain with a radius varying from 20 to 100 km is placed at the base of the model. A rectangular seed is also introduced at the crust-mantle boundary to simulate pre-existing lithospheric heterogeneity. The model parameters and their corresponding values are detailed in Table 1.

To investigate plume-rift interactions observed in various intra-plate tectonic settings, we consider four key variables in this modeling approach: (1) plume-rift distance, (2) plume radius, (3) plate velocity, and (4) lithospheric strength. It is noteworthy that plume-rift interactions have played a significant role in the tectonic evolution of the Indian subcontinent, as several mantle plumes have interacted with the Indian craton during its northward drift in geological history. These include the Kerguelen plume (~120–117 Ma), the Marion plume (~90 Ma), and the Réunion plume (~66 Ma). Geological evidence indicates that various pre-existing rift systems, such as the Narmada Rift along the western craton and the Mahanadi-Godavari Rift along the eastern craton, reactivated during the plume events (Fig. 1b). To examine their interactions under varying plate kinematics, we selected plate velocities ranging from 0.5 cm/year to 5 cm/year, representing the effects of slow and rapid drift velocities of the Indian craton on plume-lithosphere interactions. Additionally, the plume-rift distance was varied between 0 and 450 km. The radius of the initial plume domain at the model base was adjusted between 50 and 200 km to simulate plumes of varying sizes. Based on available literature data (Naliboff et al., 2020), the viscosity of the mantle lithosphere was set in the range of 5×10^{21} to 5×10^{22} Pa·s to represent the subcratonic lithosphere of the Indian region accurately.

3. 2 Reference model simulations

We conducted a series of simulation experiments to investigate how mantle plumes interact with continental lithosphere containing a pre-existing rift. The simulations reveal that plume evolution can follow one of three distinct pathways: 1) Asymmetric plume flow toward the rift, triggered by reactivation of the rift; 2) Plume stagnation, resulting from the cessation of rift activity; and 3) Plume drift, induced by the formation of a new rift. The dominance of any specific pathway is determined by the model variables (described in the previous section). Figure 2a illustrates a model simulation demonstrating the dominant rift-ward repositioning of a plume during its stagnation at the lithospheric base. In the initial stage, the buoyant plume head develops into a mushroom shape while exerting dynamic stresses on the mantle lithosphere, leading to significant surface uplift. The plume head also spreads horizontally, but this spreading is strongly asymmetric. The asymmetry arises from the pull of materials toward a low-pressure zone formed beneath the rift center. This dynamic pull also causes the plume axis to tilt toward the rift at an angle of approximately 10–15°. Subsequently, part of the plume material preferentially ascends along the reactivated rift zone, ponding beneath the rift axis (Fig. 2a). Continued material ponding and the associated decompression melting locally increase dynamic pressure, leading to stress localization that weakens the crustal portion of the lithosphere. This weakening further facilitates the reactivation of the rift system during the emplacement of underplated materials (Fig. 2a), resulting in high-amplitude (~ 20 km) upwraping of the Moho and development of negative surface topography (~ 1km) above the location of upwrapping (Fig. 2b). On the opposite flank of the plume head, the material is pulled in much smaller volumes (<25%) and fails to penetrate the crustal lithosphere. Instead, this material stagnates at the lithospheric base. After 6-7 Ma of the initial event, the plume generates a second pulse, which follows a similar evolutionary path and drifts toward the rift axis. However, this second pulse has a much weaker effect on rift reactivation due to its smaller volume, lower dynamic pressure, and reduced decompression melting. The asymmetrical spreading of the plume generates a much larger buoyancy flux (calculated as the density anomaly multiplied by horizontal velocity; Fig. 2c) on the rift-ward side compared to the opposite side. The velocity profiles show that rift-ward flows of plume material are significantly faster than those on the opposite side of the plume axis (Fig. 2d). These profiles further suggest that the rift-ward flows exhibit Poiseuille flow characteristics, with maximum horizontal velocities occurring in the middle of the asthenospheric channel. The modeled velocity field patterns align with seismic anisotropy observations from the Réunion plume (Barruol et al., 2019). Notably, the plume head spreads significantly faster than the overriding plate (Fig. 2d).

Another reference simulation is presented in Figure 3 to show the evolutionary path of a plume as it tends to stagnate at the lithospheric base. The initial stages of evolution are similar to those described earlier. However, the plume begins to deform the overlying lithosphere after stagnation, resulting in the highest surface uplift directly above the plume head (Fig. 3a, b). This contrasts with the previous model (Fig. 2a, b), where the highest surface elevations occurred symmetrically on either side of the reactivated rift axis. Additionally, the plume head spreads symmetrically around its axis in an upright position with nearly equal buoyancy flux (Fig. 3c) and lateral spreading velocities (~4 cm/yr) (Fig. 3d), suggesting a significantly weak mechanical influence of the adjacent rift. This mode of interaction concentrates stresses primarily on the oceanic plate directly above the plume axis, exerting a slight mechanical weakening effect on the pre-existing rift zone. Overall, this model predicts the generation of small melt volumes from the initial plume pulse, with subsequent pulses producing even smaller volumes.

A third reference model is presented in Figure 4 to illustrate the evolutionary path of a plume in the absence of strong influence by the pre-existing rift. Following the plume's impingement into the mantle lithosphere, the model develops maximum MOHO upwrapping above the plume head (Fig. 4b), which tilts opposite to the rift axis (Fig. 4a). This tilting is attributed to stronger frictional shear from plate motion directed away from the rift. The plume materials of the primary pulse flow horizontally away from the rift and weaken the crustal lithosphere, resulting in the formation of a new rift in the impinged region (Fig. 4a). The initiation of the new rift induces significant divergent velocities (~4cm/yr) in the crust (Fig. 4d), creating a sink for plume material to underplate beneath the newly formed rift. In contrast, the pre-existing rift fails to strongly reactivate under the transformed crustal velocity conditions (Fig.4b), allowing the left flank of the plume to evolve with higher buoyancy fluxes and achieve maximum velocities (Fig. 4c). This model highlights the role of plate motion in reversing the flow direction in the lithosphere, as reflected in the velocity profiles (Fig. 4d). At 3 Ma, the horizontal component of plate velocity entirely dictates the magnitude of horizontal flows (2-3 cm/yr) in the plume material at the lithospheric base. This finding contrasts sharply with observations from the first reference simulation (Fig. 2a), where plume materials flowed counter to the plate motion due to pressure drag from the reactivated pre-existing rift. Over time, however, the plume spreading velocity surpasses the plate velocity, dominating the system's dynamics (Fig. 4d). This plume-dominated dynamics eventually forms a new rift at the point of flow divergence, which ceases the pre-existing rift activity.

3.3. Rift-plume interactions: parametric analyses

3.3.1 Plume axis - rift separation (δ)

We varied the horizontal distance (δ) between the lithospheric pre-existing weak zone (rift) and the plume axis in the model runs, keeping all other model parameters constant. For a large plume-rift distance (δ = 250 Km), the plume ascends through upper mantle to vertically encounter the lithospheric base at 0.8 Ma, producing nearly symmetrical flow divergence above the plume head (Fig. 5a). During this interaction, the ascending plume induces upward flexural deformations in the lithosphere, developing high strain-rates in the crustal layer right above the plume axis. The pre-existing rift zone, however, remains under a low strain-rate condition, showing little or no reactivation (as indicated by a decreasing strain rate in Fig. 5b). The first plume pulse progressively attains an active phase (1 Ma – 4 Ma) of stagnation in which the plume head migrates dominantly in the horizontal direction, dragging basal lithospheric materials to subduct symmetrically at either flank of the plume. At 1.29 Myr, the plume generates a second pulse, which similarly interacts with the lithosphere, leading to significant thinning of the mantle lithosphere. This pulse also produces a high- strain zone, aligned slightly off-axis with respect to the plume structure in the direction of rifting plate motion. From the model velocity field, it appears that the reactivation of the rift forces the plume head to impinge asymmetrically further into the lithosphere. Overall, they are characterised by low buoyancy flux ratio and low-velocity ratio beneath the original rift (Fig. 5c, d).

Model with δ = 200 Km shows a similar evolutionary trend of the plume head prior to its encounter with the lithospheric base at 0.9 Myr. After impinging to the lithosphere, plume materials flow laterally in both directions towards and away from the rift axis. The plume impingement gives rise to a high-strain zone in the lithosphere directly above the plume axis, as observed in the δ = 200 Km model (Fig. 5b). However, strong lateral flows cause this high-strain zone to disappear within a short period of time (1.2 Myr). The divergence motion in the plume drags the overlying lithospheric materials to flow in the horizontal directions above the stagnated plume material. Consequently, the plume dynamics becomes too weak to impinge into the lithosphere further. Further decrease in δ (= 150 Km) drastically changes the pattern of plume-lithosphere interaction. Unlike the previous model, this model develops strongly asymmetric high-strain zones in the lithosphere when the plume tends to interact with the overlying lithosphere (Fig. 5b). The high-strain zones are characteristically aligned toward the rifting axis. The rift reactivation eventually pulls the impinging plume materials to accumulate beneath the rift axis and induces strong upwrapping of the Moho. However, the plume materials stagnated at the lithospheric base flow horizontally at higher rates to develop stronger drags to the lithosphere on the flank opposite to rift axis, resulting in asymmetric delamination of lithospheric mantle. Overall, they are characterised by a very high buoyancy flux ratio and high-velocity ratio beneath the original rift (Fig. 5c, d).

3.3.2 Divergent velocity in rifting (V_p)

We ran a set of simulations by varying the pull velocity (V_p) at the edges of the model lithospheric plate, keeping the plume-rift distance δ was held constant at 200 Km. For V_p = 0.5cm/year, the plume head ascends at a 2 cm/year rate to encounter the lithospheric base at 0.9 Myr. Its impingement into the lithosphere forces the plume materials to flow laterally towards and away from the rift axis. This divergent flow pattern drags the overlying lithospheric mantle, eventually delaminating and subducting at either plume flank. Increasing V_p accelerates the ascent rate (4 cm/year) of the plume, allowing the plume to interact with the lithosphere at a relatively shorter time (~ 0.8 Myr). The plume materials begin to spread divergently in horizontal directions upon impingement, as in the previous model. The second plume pulse produced after 3 Myr significantly weakens the lithosphere, leading to off-axial emplacement of a part of the plume materials in the direction of plate motion. Large V_p values (~5 cm/year) causes the plume head to become strongly asymmetrical before it interacts with the lithosphere (Fig. 5d). This symmetric to asymmetric transition of the plume head occurs due to a more substantial drag of rift-ward mantle flows driven by the reactivation of the rift as well as the high buoyancy flux beneath the rift (Fig. 5c). The rift-controlled kinematics forces the plume head toward the rift. After impinging into the base, the plume materials continue to flow toward the rift, ultimately channelizing through the rift axis in the lithosphere and give rise to large upwrapping of the Moho.

4.3. Interacting versus non-interacting rift-plume systems

Using a synthesis of the model results, we recognize three distinct plume-rift mechanisms: 1) Mechanism I- plume-induced reactivation of pre-existing rift and its feedback effect on rift-ward plume flow, 2) Mechanism II- plume stagnation at lithospheric base, accompanied by cessation of the pre-existing rift, and 3) Mechanism III- plume-induced neo-rifting in lithosphere, and its influence in plume remobilization. Each of these three mechanisms becomes operational under specific conditions of the following factors: horizontal separation between the plume axis and the pre-existing rift (δ), viscosity (η_L) of the overlying mantle lithosphere, continental plate velocity (V_p), and initial plume size (R) (Fig. 6). Small δ, or high V_p or large R gives rise to the plume tectonic setting to evolve in Mechanism I, favouring the pre-existing rift to reactivate and pull most of the plume material to accumulate beneath its axial zone. This mechanism activates the pre-existing rift in determining the location of plume-driven volcanism away from the plume axis, as applicable for Deccan volcanisms. Our model suggests that the main eruption site of this volcanic event in the Indian craton was located away from the Reunion plume axis due to intense plume-rift interaction in Mechanism I. Increasing δ or V_p, or decreasing plume size lowers the plume-rift interaction, resulting in a transition from Mechanism I to III. Mechanism III allows a large volume fraction of the plume materials to flow in the direction opposite to the pre-existing rift. This condition fails to reactivate the rift but gives rise to new rifts in the overlying lithosphere, depending on η. The transitional mechanism (Mechanism II) stagnates plume materials at the lithospheric base, and the rift-ward flows become progressively weak, leading to the cessation of the pre-existing rift activities.

Mechanisms I (interacting plume-rift setting) and II (non-interacting plume-rift setting) yield contrasting melt generation patterns. An interacting system evolves through higher degrees of decompression melting, with the resulting melt potentially reaching the surface depending on the availability of fracture systems during the reactivation of the pre-existing rift. On the other hand, non-interacting systems can produce substantial amounts of melts when the overlying lithosphere is weak, allowing the plume materials to ascend to shallower depths (Figs. 2a & 4a). Moreover, the present study reveals that these two mechanisms give rise to distinctive surface topography with significant differences in the Moho profiles (Figs. 2b & 4b). Plume underplating and melt generation result in the unwrapping of Moho and the formation of a topographic high directly above the plume head in non-interacting conditions. However, plume-rift interaction adds complexities to the topographic response. The topography progressively subsides in rift reactivation, attaining more negative elevations over time, while the Moho depth decreases. As the plume encounters the lithosphere, the plume head starts to spread laterally and reactivate the rift system, which further reduces the surface topography and Moho depth, but in an asymmetric fashion in the case of an interacting plume-rift system. The old rift remains dormant for non-interacting systems, and a topographic low and Moho unwrapping occurs in the new rift location.

4. Discussions

4.1. Deccan volcanic materials in rifted basins: model interpretations

We discuss the model results in the context of how the pre-existing rifts in the Indian peninsula might have affected the Reunion plume in its encounter with the Indian continental lithosphere. Considering the plume – continental lithosphere interactions obtained from the model simulations, we suggest that a part of the plume (<10 % of the total plume head volume) contributed to material supply for the magma generation during the Deccan volcanic event (Fig. 2a). Our model results indicate that the rift reactivation can split the plume head, and drag a part of it to the rift zone when the rift-plume distance is significantly close (< 200 km). The rift-plume distance calculated from their paleo-pole positions corresponding to the timing of Deccan volcanism supports our proposition that the occurrence of continental rifts significantly influenced the plume stagnation and its repositioning at the lithospheric base. The northward drifting Indian landmass progressively increased its distance from the Reunion plume, ceasing the rift-plume interaction. From the model results, we suggest attaining this non-interaction state after the main phase when the rift –plume distance became > 400 km (Fig. 6).

We chose a mantle plume of equivalent size (~150 km) in our model to simulate the Indian tectonic setting controlled by the Reunion plume activity beneath the Indian craton. The model introduces a pre-existing rift at a distance similar to that between the Reunion plume and CITZ around ~75-66 Ma. Our model results suggest that during Deccan volcanism the plume was close enough to reactivate the Narmada-Tapti rift, resulting in drifting of a part of the plume towards the rift, which eventually produced a substantial amount of partial melts required for underplating and subsequent magmatism along the rift zone (Fig. 2a). The topographic highs and lows observed in our model closely match with the topographic undulations in the Indian craton attributed to the Reunion activity (Fig. 2b), as reported by several authors (Ghosh, 2015; Kumar et al., 2015; Prasad et al., 2018). Additionally, the model findings indicate that Moho upwarping beneath the plume offshoots (Fig. 2b) corresponds well with the elevated Moho depth observed in regions of positive Bouguer gravity anomalies (Kumar et al., 2015; Singh, 1998).

4.2 The Narmada-Son rift and the Reunion plume: their interactions

The Narmada-Son lineament (NSL) is an intensely deformed E-W trending tectonic zone from 72.5∘E to 82.5∘E. The lineament forms a prominent linear tectonic feature in the western part of the Indian subcontinent (Fig. 7a). Some studies consider the NSL as a suture zone between two contrasting geological terrains: the Bundelkhand proto-continent to the north and the Dharwar proto-continent to the south of it (Choubey, 1971). In a broader perspective, the NSL occurs in the Central Indian Tectonic Zone, which is recognized as a collision zone to account for the amalgamation of Singhbhum, Bastar, and Dharwar cratons in the south and the Bundelkhand craton in the north during the late Archean time (Jain et al., 1995). A group of authors claim that the NSL is a continental rift zone which has experienced reactivation multiple times since the Proterozoic (e.g., Choubey, 1971). From the available geophysical data, Mishra (1977) identifies the NSL as a typical rift structure, extending up to the Murray ridge in the Arabian Sea (Fig. 7a). Biswas and Deshpande (1983), based on geological evidence, further correlated this rift with the East African rifts.

A direction of earlier studies suggests that the stratigraphic signatures of NSL is akin to a horst-type tectonic setting, bordered by the Son-Narmada and the Tapti faults to its north and south, respectively (Qureshy, 1982). The regional gravity anomaly pattern locates the Tapti-Narmada-Son zone as a broad region of gravity high, in which the NSL occurs as a narrow zone of low gravity (Qureshy, 1982). There are two major seismically active faults: the Narmada south fault (NSF) and the Narmada north fault (NNF) (Fig. 7a), bounding the NSL. The origin of NSF and NNF is traced back to the middle to late Archaean tectonic events (Choubey, 1971; Jain et al., 1995). To the north of NSL lies Precambrian terrains: the Vindhyan basin (750–1721 Ma) and the Bundelkhand craton (2.5 Ga), whereas much younger units, the Deccan volcanics (~65 Ma old) on the south (Singh 2015).

The high Bouguer gravity anomalies in the NSL are attributed to high-density materials in the lower crust, which were emplaced by large-scale asthenospheric upwelling (Singh, 1998). Interestingly, Rai et al., (2005) report a 52 km Moho downwarp across the lineament, whereas an average Moho depth of 40 km elsewhere in the Indian craton. Additionally, the crust beneath the NSL yields V_p/V_s ratios (1.84) significantly higher than those (1.73) in the surrounding regions. These geophysical observations support the possibility of a high-density mafic mass at depth compensating the crustal root, as reflected in a small topographic variation (200 m) across the lineament. To explain the cause of the seismically active current state, the authors suggest that the presence of such an anomalous mass in the deep crust perhaps developed gravity-induced stresses in the lower crust, resulting in crustal failure along the pre-existing Narmada-Son fault to generate earthquakes.

Our model results show that plume materials can flow laterally toward a rift if the lithosphere is sufficiently strong (viscosity > 10^{22} Pa s), or the plate drifts at fast rates (> 4cm/year) (Fig. 6). It is to be noted that both the conditions are valid for the Indian plate tectonic setting. This rift-driven flow eventually led to the accumulation of plume materials in the asthenosphere beneath the rift zone. They underwent partial melting and underplating beneath the NSL (Fig. 7b), as inferred from positive Bouger anomaly within this region. The model findings also indicate that the northward rapid movement of the Indian plate forced the plume head to tilt in the upper mantle by a significant amount, which further facilitated the rift-ward migration of the plume materials. Model calculations indicate that the lateral drift velocity of the plume reached ~ 10 cm/year, implying that the plume materials took approximately 8-10 Myr to reach the basement of NSL and Cambay basin.

4.3. Godavari and Mahanadi rifts: influence of the Reunion plume

Godavari rift consists of three major faults (WNW-ESE trending Kadam fault (KF); the Kinnerasani Godavari fault (KGF); the Godavari valley fault (GVF) that adjoin the rift, suggest recent tectonic activities evidenced by moderate levels of seismicity (Fig. 8a) (Chaudhuri and Deb, 2003). Geophysical studies show a prominent increase in crustal thickness in the rift (Fig. 8b), marked by a sudden increase in seismic wave velocity and a weak Moho (Kaila et al., 1990; Singh et al., 2012) with respect to that in the Eastern Dharwar craton. The geophysical anomalies are associated with a high heat-flow rate in the rift region (Fig. 8c) (Singh et al., 2015). However, the craton displays the mantle transition zone at 410 and 660 km transition zone beneath the rift (Singh et al., 2012), as expected normally. These observations rule out the possibility of a deep-mantle upwelling zone beneath the Godavari rift, instead suggest the occurrence of a sill-like intrusion, which can justify the rheological contrast (high seismic wave velocity), Moho downwraping and the lower availability of partial melts in this region. Our model results for a moderate plume-rift distance comply with these findings, suggesting that the plume materials spread out asymmetrically under the rift influence and underplate at the lithospheric base beneath the rift region (Fig. 8d). The underplating eventually gives rise to high heat flow and an overall increase in crustal thickness, as found beneath the Godavari rift region. The underplated plume materials were depleted, resulting in lower degrees of partial melting beneath the rift, as revealed by the geological sequences in the Godavari rift region.

Unlike the NSL and Cambay basins, the Mahanadi rifts display signatures of underplating and subsequent volcanisms of early Cretaceous, which are, however, linked to the earlier Kerguelen plume event (Behera et al., 2004). However, the mode of their plume-rift interaction was similar to that described for the Reunion plume, leading to an offset of the Kerguelen plume from the Indian craton. As the Indian plate moved due north-west during this Kerguelen event, the plume materials of the Kerguelen hotspot were dragged towards the rifts to underplate at the base of the Mahanadi rift, leading to upwrapping of the Moho, as revealed from geophysical studies (Basantaray and Mandal, 2022; Behera et al., 2004). No such evidence of interaction was found since the late Cretaceous time, and the Mahanadi rift has remained dormant most of the Cenozoic. From our model, we decipher that the plume-rift distance between the Réunion plume and Mahanadi rift at 66 Ma was large compared to the NSL and Godavari rift. Thus, The Mahanadi rift had a weak interaction with the Reunion plume, resulting in no underplating of the plume materials, as observed in the present model and supported by geophysical evidence (Behera et al., 2004).

5. Conclusions

Using 2D thermomechanical numerical models, this study provides new insights into the modes of plume–rift interaction in a continental tectonic setting, which explains the interplay between the Réunion plume event and the palaeo-rift system in the Indian craton. The model results suggest that the interaction depends primarily on the lateral distance between the plume and the rift and the lithospheric plate velocity. Small plume-rift distance or high plate velocity empowers the pre-existing rift in pulling a substantial amount of fertile plume materials to accumulate beneath the rift axis, which eventually undergoes partial melting, leading to the reactivation of the rift system due to the higher buoyancy flux. For a large plume-rift distance or low plate velocity, on the other hand, the plume materials escape the rift-pull, and underplate beneath the lithospheric base with little or no melt production, leaving the rift system without any reactivation. These model findings suggest that the Narmada-Tapti rift, which was close to the Réunion hotspot during Cretaceous time, forced a large amount of plume materials to drift towards the rift. The fertile plume materials then underwent melting, resulting in Moho upwrapping due to their high buoyancy flux and subsequent reactivation of the palaeorift. The Godavari basin, located further away from the plume epicentre during this time, had little influence from the Reunion plume and thereby did not involve any significant melting as the plume materials were depleted. The Godavari rift setting led to the underplating of the plume head at the lithospheric base, followed by Moho downwraping as the buoyancy flux was relatively low. These model interpretations are aligned with the geophysical observations that suggest the occurrence of partial melts beneath the Narmada-Tapti region, with significant underplating and noticeable crustal thickening beneath the Godavari rift.

Acknowledgment

The present work has been supported by the DST-SERB through the J. C. Bose fellowship (JBR/2022/000003) to NM and an INSPIRE Faculty Fellowship (DST/INSPIRE/04/2022/002647) granted by Department of Science and Technology (DST), India, to DG. JS is thankful to DST-INSPIRE for the senior research fellowship (IF170697). The Computational Infrastructure for Geodynamics (geodynamics.org), funded by the National Science Foundation under awards EAR-0949446 and EAR-1550901 is acknowledged for supporting the development of ASPECT

Declaration of Interest Statement

The authors declare that they have no known competing financial interests or personal relationships that could have appeared to influence the work reported in this paper.

Appendix A

A.1 Governing equations

The code used for our numerical simulations is ASPECT, a massively parallel finite element code primarily designed for modeling thermal convection in the mantle. It consists of a small core that solves the basic fluid dynamics equations, and for other tasks, it relies on external libraries and plug-ins (Bangerth et al., 2022a, 2022b; Heister et al., 2017; Kronbichler et al., 2012). The code is based on the DEAL.II software library (Alzetta et al., 2018) and assumes that, at a regional length scale and geological time scale, earth materials may be treated as highly viscous fluid with infinite Prandtl number, and hence Stokes equations can be solved neglecting inertial forces. This leads to the following expression of the momentum equation:

$$-\nabla.\left(2\mu_{eff}\dot{\epsilon}(u)\right)+\nabla P=\rho g \tag{1}$$

where μ_{eff} is the effective viscosity, $\dot{\epsilon}$ is the strain rate tensor, $u$is the velocity vector, ρ is the density, and $g$is the gravity vector. Materials the assumed incompressible leading to zero divergences of the velocity vector u:

$$\nabla.u=0 \tag{2}$$

The effect of the temperature field should also be taken into account using the conservation of energy equation:

$$\rho C_P\left(\frac{\partial T}{\partial t}+u.\nabla T\right)-\nabla.\left(k+\upsilon_h(T)\right)\nabla T=H_r \tag{3}$$

where C_P is the heat capacity, T is temperature, k is thermal conductivity, and H_r is the internal radiogenic heat production. υ_h is the artificial diffusivity that prevents the oscillations due to advection of the temperature field calculated following entropy viscosity method.

To account for the advection of material properties, ASPECT relies on compositional fields that are advected with the flow (Gassmöller et al., 2018). Hence, the system of equations is closed by solving for a conservation equation for each compositional field as:

$$\frac{\partial c_i}{\partial t}+u.\nabla c_i-\nabla.\left(\upsilon_h(c_i)\right)\nabla c_i=0 \tag{4}$$

where c_i is the i^{th} compositional field. Artificial viscosity is again introduced to stabilize advection.

A.2 Constitutive nonlinear rheology

In ASPECT, material properties are implemented within the *Material model* module, which adapts a visco-plastic rheology. The model is incompressible and depends primarily on diffusion-dislocation and Drucker-Prager criterion, which can be combined into more complex rheologies.

At higher temperatures, materials experience nonlinear viscous deformation via power-law dislocation creep or grain boundary (or bulk) diffusion creep. These two rheologies can be expressed by strain rate and temperature-dependent viscosity as:

$$\mu_{eff}^{vis} = \frac{1}{2} A^{\frac{-1}{n}} d^{\frac{m}{n}} \dot{\epsilon}_{ii}^{\frac{(1-n)}{n}} exp\left(\frac{E + PV}{nRT}\right) \tag{5}$$

where A is the prefactor, n is the stress exponent, $\dot{\epsilon}_{ii} = \sqrt{\frac{1}{2}\dot{\epsilon}'_{ij}\dot{\epsilon}'_{ij}}$ is the effective deviatoric strain rate, which is the square root of second invariant of deviatoric strain rate tensor, d is the grain size, m is the grain size exponent, E is the activation energy, V is the activation volume and R is the gas constant. In case of diffusion creep (μ_{eff}^{df}), n =1 and m>0, while for dislocation creep (μ_{eff}^{dl}) n>1 and m=0.

At relatively low temperature the material behavior is modelled using plastic rheology. The effective viscosity is locally adapted so that the stress generated during deformation does not exceed the yield stress (viscosity rescaling method). The effective plastic viscosity is given by

$$\mu_{eff}^{pl} = \frac{\sigma_y}{2\dot{\epsilon}_{ii}} \tag{6}$$

where σ_y is the yield stress. Here, plasticity limits viscous stress via Drucker-Prager yield criterion given by:

$$\sigma_y = C cos(\varphi) + P sin(\varphi) \tag{7}$$

where *C* is the cohesion and φ is the friction angle. This 2D form of the equation is equivalent to Mohr Coulomb yield surface and for $\varphi = 0$, the yield stress is fixed and equal to cohesion (Von Mises yield criterion).

In nature, under the same deviatoric stress, both viscous creeps act simultaneously. Hence, we consider composite viscous rheology by harmonically averaging μ_{eff}^{dl} and μ_{eff}^{df}

$$\mu_{eff}^{cp} = \frac{\mu_{eff}^{df}\mu_{eff}^{dl}}{\mu_{eff}^{df} + \mu_{eff}^{dl}} \tag{8}$$

Moreover, we assume that the viscous creep and plastic yielding are independent processes that can occur simultaneously, and the mechanism resulting in the lowest effective viscoplastic stress is favored:

$$\mu_{eff}^{vp} = min\left(\mu_{eff}^{pl}, \mu_{eff}^{cp}\right) \tag{9}$$

Strain weakening is included in the system by calculating the finite strain invariant through compositional fields within the material model and linearly reducing the cohesion and internal friction angle as a function of the finite strain magnitude. While calculating finite strain invariant (e_{ii}), a single composition field tracks the value of finite strain invariant via

$$e_{ii}^{t} = e_{ii}^{(t-1)} + \dot{e}_{ii}dt \tag{10}$$

where *t* and *t-1* are current and prior time steps, $\dot{e}_{ii}$ is the second invariant of the strain rate tensor, and *dt* is the time step size. When the accumulated strain is less than a given value, *C* and φ are constant. For accumulated strain values greater than this threshold, *C* and φ decrease linearly until the system reaches a certain maxima of accumulated strain is reached, after which they are kept constant again (Table 2).

A.3 Model parameters and boundary conditions

To solve a model problem in ASPECT, our domain is discretized into quadrilateral finite elements. Basis functions are then defined for the independent variables such as velocity, pressure, temperature and compositional fields. Here, we employ second-order polynomials for velocity, first-order polynomials for pressure (Q_2Q_1 elements), and second-order polynomials for temperature and composition. We have always used a square grid to solve our problem where all the cells have the same height and width. The model domain is subdivided in such a way that it has a finite element grid with uniform 2 km spacing.

The initial temperature profile is adiabatic with a potential temperature of 1600 K. This adiabatic profile is superimposed with a conductive temperature profile for the continental lithosphere. If the layer has thickness *dz,* then the temperature at, and heat flow through, the bottom of the layer (T_B, q_B) can be expressed in terms of the temperature and heat flow at the top of the layer (T_r, q_r) and properties (A,k) of the layer,

$$T_B = T_T + \frac{q_T}{k}\Delta z - \frac{A\Delta z^2}{2k} \tag{11}$$

$$q_B = q_T - A\Delta z \tag{12}$$

Equations (11) and (12) are applied to successive layers, resetting T_T and q_T at the top of each new layer with the values T_B and q_B solved for the bottom of the previous layer. A temperature perturbation of 200 K is added to the plume material at of the bottom boundary of the model.

The density is primarily dependent on the composition, but in a compressible medium, it also depends on pressure and temperature, whereas in an incompressible medium, it depends only on temperature. The density depends on pressure and temperature via the following two equations:

$$\rho_{incomp} = \rho_{ref}\left(1 - \alpha\left(T - T_{ref}\right)\right) \tag{13}$$

$$\rho_{comp} = \rho_{ref}\left(\beta\left(P - P_{surface}\right)\right)\left(1.0 - \alpha\left(T - T_{ref}\right)\right) \tag{14}$$

Since our visco-plastic model is incompressible in nature, the density variation will follow eq(13).

A viscosity profile is also needed to model plume and lithosphere interaction properly. The viscosity is calculated in ASPECT using flow laws given in section A.2. They depend on pressure, temperature, and strain rate. Our profile has a high viscosity upper crust followed by a relatively low viscosity lower crust, which follows a lithospheric mantle whose viscosity gradually decreases from high (equivalent to upper crust) to moderate due to an increase in temperature. This is followed by the upper mantle, which has even lower viscosity.

The boundary composition and temperature are the same as the initial composition and temperature. The bottom boundary is *free slip* and *isothermal,* with a maximum temperature of 1700 K. The top boundary is a *free surface* (or *free slip*) and *isothermal* with a minimum temperature of 293 K (or 273 K) (Table 1). The side boundaries are *insulating* in nature. A prescribed diverging velocity profile of 0.25 cm/year to 5 cm/year is given in the lithosphere, which is well within the limit of slow-spreading ridge (Table 1). The vertical velocity on the side boundaries of the lithosphere is zero. This mass outflux through the lithosphere is counter balanced by mass influx in the mantle to conserve total mass.

References

Alzetta, G., Arndt, D., Bangerth, W., Boddu, V., Brands, B., Davydov, D., Gassmöller, R., Heister, T., Heltai, L., Kormann, K., Kronbichler, M., Maier, M., Pelteret, J.P., Turcksin, B., Wells, D., 2018. The deal.II library, Version 9.0. Journal of Numerical Mathematics 26, 173–183. https://doi.org/10.1515/jnma-2018-0054

Baksi, A.K., 1995. Petrogenesis and timing of volcanism in the Rajmahal flood basalt province, northeastern India. Chem Geol 121, 73–90.

Bangerth, W., Dannberg, J., Fraters, M., Gassmoeller, R., Glerum, A., Heister, T., Myhill, R., Naliboff, J., 2022a. ASPECT v2.4.0. https://doi.org/10.5281/zenodo.6903424

Bangerth, W., Dannberg, J., Fraters, M., Gassmoeller, R., Glerum, A., Heister, T., Myhill, R., Naliboff, J., 2022b. Advanced Solver for Problems in Earth's ConvecTion, User Manual. https://doi.org/10.6084/m9.figshare.4865333

Basantaray, A.K., Mandal, A., 2022. Interpretation of gravity–magnetic anomalies to delineate subsurface configuration beneath east geothermal province along the Mahanadi rift basin: a case study of non-volcanic hot springs. Geothermal Energy 10. https://doi.org/10.1186/s40517-022-00216-4

Behera, L., Sain, K., Reddy, P.R., 2004. Evidence of underplating from seismic gravity studies in the Mahanadi delta eastern India and its tectonic significance. J Geophys Res Solid Earth 109, 1–25. https://doi.org/10.1029/2003JB002764

Bhattacharji, S., Chatterjee, N., Wampler, J.M., Nayak, P.N., Deshmukh4, S.S., 1996. Indian Intraplate and Continental Margin Rifting, Lithospheric Extension, and Mantle Upwelling in Deccan Flood Basalt Volcanism near the K/T Boundary: Evidence from Mafic Dike Swarms1. J Geol 104, 379–398.

Bhowmik, S.K., Wilde, S.A., Bhandari, A., Pal, T., Pant, N.C., 2012. Growth of the Greater Indian Landmass and its assembly in Rodinia: Geochronological evidence from the Central Indian Tectonic Zone. Gondwana Research 22, 54–72. https://doi.org/10.1016/j.gr.2011.09.008

Blackburn, T.J., Olsen, P.E., Bowring, S.A., Mclean, N.M., Kent, D. V, Puffer, J., Mchone, G., Rasbury, E.T., Et-Touhami, M., 2013. Zircon U-Pb Geochronology Links the End-Triassic Extinction with the Central Atlantic Magmatic Province. Science (1979) 340, 941–945.

Bryan, S.E., Ferrari, L., 2013. Large igneous provinces and silicic large igneous provinces: Progress in our understanding over the last 25 years. Bulletin of the Geological Society of America. https://doi.org/10.1130/B30820.1

Burov, E., Gerya, T., 2014. Asymmetric three-dimensional topography over mantle plumes. Nature 513, 85–89. https://doi.org/10.1038/nature13703

Burov, E., Guillou-Frottier, L., 2005. The plume head-continental lithosphere interaction using a tectonically realistic formulation for the lithosphere. Geophys J Int 161, 469–490. https://doi.org/10.1111/j.1365-246X.2005.02588.x

Chattopadhyay, A., Bhowmik, S.K., Roy, A., 2020. Tectonothermal evolution of the Central Indian Tectonic Zone and its implications for Proterozoic supercontinent assembly: The current status. Episodes 43, 132–144. https://doi.org/10.18814/epiiugs/2020/020008

Chaudhuri, A.K., Deb, G.K., 2003. Proterozoic Rifting in the Pranhita-Godavari Valley: Implication on India-Antarctica Linkage. Gondwana Research 7, 301–312.

Chenet, A.L., Quidelleur, X., Fluteau, F., Courtillot, V., Bajpai, S., 2007. 40K-40Ar dating of the Main Deccan large igneous province: Further evidence of KTB age and short duration. Earth Planet Sci Lett 263, 1–15. https://doi.org/10.1016/j.epsl.2007.07.011

Choubey, V.D., 1971. Narmada-Son Lineament, India. Nature 232, 38–40.

Curray, J.R., Munasinghe, T., 1991. Origin of the Rajmahal Traps and the 85°E Ridge: Preliminary reconstructions of the trace of the Crozet hotspot. Geology 19, 1237–1240.

Ernst, R.E., 2014. Large Igneous Provinces. Cambridge University Press.

François, T., Koptev, A., Cloetingh, S., Burov, E., Gerya, T., 2018. Plume-lithosphere interactions in rifted margin tectonic settings: Inferences from thermo-mechanical modelling. Tectonophysics 746, 138–154. https://doi.org/10.1016/j.tecto.2017.11.027

French, S.W., Romanowicz, B., 2015. Broad plumes rooted at the base of the Earth's mantle beneath major hotspots. Nature 525, 95–99. https://doi.org/10.1038/nature14876

Funck, T., Jackson, H.R., Louden, K.E., Klingelhöfer, F., 2007. Seismic study of the transform-rifted margin in Davis Strait between Baffin Island (Canada) and Greenland: What happens when a plume meets a transform. J Geophys Res Solid Earth 112. https://doi.org/10.1029/2006JB004308

Gassmöller, R., Lokavarapu, H., Heien, E., Puckett, E.G., Bangerth, W., 2018. Flexible and Scalable Particle-in-Cell Methods With Adaptive Mesh Refinement for Geodynamic Computations. Geochemistry, Geophysics, Geosystems 19, 3596–3604. https://doi.org/10.1029/2018GC007508

Ghosh, D., Sen, J., Mandal, N., 2024. Periodicity in the Deccan Volcanism Modulated by Plume Perturbations at the Mid-Mantle Transition Zone. J Geophys Res Solid Earth 129. https://doi.org/10.1029/2024JB029020

Ghosh, G.K., 2015. Interpretation of Gravity Anomaly and Crustal Thickness Mapping of Narmada-Son Lineament in Central India. Journal of Geological Society of India 86, 263–274.

Gibson, S.A., Thompson, R.N., Leonardos, O.H., Dickin, A.P., Mitchell, J.G., 1999. The limited extent of plume-lithosphere interactions during continental flood-basalt genesis: geochemical evidence from Cretaceous magmatism in southern Brazil. Contributions to Mineralogy and Petrology 137, 147–169.

Glišović, P., Forte, A.M., 2017. On the deep-mantle origin of the Deccan Traps. Science (1979) 355, 613–616. https://doi.org/10.1126/science.aah4390

Heister, T., Dannberg, J., Gassmöller, R., Bangerth, W., 2017. High accuracy mantle convection simulation through modern numerical methods - II: Realistic models and problems. Geophys J Int 210, 833–851. https://doi.org/10.1093/gji/ggx195

Issachar, R., Haas, P., Augustin, N., Ebbing, J., 2024. Rift and plume: a discussion on active and passive rifting mechanisms in the Afro-Arabian rift based on synthesis of geophysical data. Solid Earth 15, 807–826. https://doi.org/10.5194/se-15-807-2024

Ito, G., Lin, J., Graham, D., 2003. Observational and theoretical studies of the dynamics of mantle plume-mid-ocean ridge interaction. Reviews of Geophysics 41. https://doi.org/10.1029/2002RG000117

Jain, S.C., Nair, K.K.K., Yedekar, D.B., 1995. Geology of the Son-Narmada-Tapti lineament zone in Central India.

Ju, W., Hou, G., Hari, K.R., 2013. Mechanics of mafic dyke swarms in the Deccan Large Igneous Province: Palaeostress field modelling. J Geodyn 66, 79–91. https://doi.org/10.1016/j.jog.2013.02.002

Kaila, K., Murty, P., Mall, D., Dixit, M., Sarkar, D., 1987. Deep seismic soundings along Hirapur-Mandla profile, central India. Geophysical Journal of the Royal Astronomical Society 89, 399–404.

Kaila, K.L., Murty, P.R.K., Rao, V.K., Venkateswarlu, N., 1990. Deep seismic sounding in the Godavari Graben and Godavari (coastal) Basin, India. Tectonophysics 173, 307–317.

Keller, G., Adatte, T., Bhowmick, P.K., Upadhyay, H., Dave, A., Reddy, A.N., Jaiprakash, B.C., 2012. Nature and timing of extinctions in Cretaceous-Tertiary planktic foraminifera preserved in Deccan intertrappean sediments of the Krishna-Godavari Basin, India. Earth Planet Sci Lett 341–344, 211–221. https://doi.org/10.1016/j.epsl.2012.06.021

Keller, G., Adatte, T., Gardin, S., Bartolini, A., Bajpai, S., 2008. Main Deccan volcanism phase ends near the K-T boundary: Evidence from the Krishna-Godavari Basin, SE India. Earth Planet Sci Lett 268, 293–311. https://doi.org/10.1016/j.epsl.2008.01.015

Kendall, J.-M., Pilidou, S., Keir, D., Bastow, I.D., Stuart, G.W., Ayele, A., 2006. Mantle upwellings, melt migration and the rifting of Africa: insights from seismic anisotropy. Geological Society, London, Special Publications 259, 55–72.

Kendall, J.M., Stuart, G.W., Ebinger, C.J., Bastow, I.D., Keir, D., 2005. Magma-assisted rifting in Ethiopia. Nature 433, 146–148. https://doi.org/10.1038/nature03161

Kinchid, C., Ito, G., Gable, C., 1995. Laboratory investigation of the interaction of off-axis mantle plumes and spreading centres. Nature 376, 758–761.

Koppers, A.A.P., Becker, T.W., Jackson, M.G., Konrad, K., Müller, R.D., Romanowicz, B., Steinberger, B., Whittaker, J.M., 2021. Mantle plumes and their role in Earth processes. Nat Rev Earth Environ. https://doi.org/10.1038/s43017-021-00168-6

Krishna, K.S., Abraham, H., Sager, W.W., Pringle, M.S., Frey, F., Gopala Rao, D., Levchenko, O. V., 2012. Tectonics of the Ninetyeast Ridge derived from spreading records in adjacent oceanic basins and age constraints of the ridge. J Geophys Res Solid Earth 117. https://doi.org/10.1029/2011JB008805

Kronbichler, M., Heister, T., Bangerth, W., 2012. High accuracy mantle convection simulation through modern numerical methods. Geophys J Int 191, 12–29. https://doi.org/10.1111/j.1365-246X.2012.05609.x

Kumar, M.R., Singh, A., Kumar, N., Sarkar, D., 2015. Passive seismological imaging of the Narmada paleo-rift, central India. Precambrian Res 270, 155–164. https://doi.org/10.1016/j.precamres.2015.09.013

Larsen, H., Saunders, A., 1998. Tectonism and volcanism at the southeast Greenland rifted margin: a record of plume impact and later continental rupture. Proceedings of the Ocean Drilling Program, Scientific Results 152.

Marzoli, A.M., Renne, P.R., Piccirillo, E.M., Ernesto, M., Bellieni, G., Min, A.D., 1999. Extensive 200-Million-Year-Old Continental Flood Basalts of the Central Atlantic Magmatic Province. Science (1979) 284, 616–618.

Mchone, J.G., 2000. Non-plume magmatism and rifting during the opening of the central Atlantic Ocean, Tectonophysics.

Meert, J.G., Pandit, M.K., Pradhan, V.R., Banks, J., Sirianni, R., Stroud, M., Newstead, B., Gifford, J., 2010. Precambrian crustal evolution of Peninsular India: A 3.0 billion year odyssey. J Asian Earth Sci 39, 483–515. https://doi.org/10.1016/j.jseaes.2010.04.026

Mishra, D.C., 1977. Possible extensions of the Narmada-Son lineament towards Murray Ridge (Arabian Sea) and the eastern syntaxial bend of the Himalayas. Earth Planet Sci Lett 36, 301–308.

Mittelstaedt, E., Ito, G., Van Hunen, J., 2011. Repeat ridge jumps associated with plume-ridge interaction, melt transport, and ridge migration. J Geophys Res Solid Earth 116. https://doi.org/10.1029/2010JB007504

Morgan, W.J., 1978. Rodriguez, Darwin, Amsterdam, ..., A second type of Hotspot Island. J Geophys Res Solid Earth 83, 5355–5360. https://doi.org/10.1029/jb083ib11p05355

Naliboff, J.B., Glerum, A., Brune, S., Péron-Pinvidic, G., Wrona, T., 2020. Development of 3-D Rift Heterogeneity Through Fault Network Evolution. Geophys Res Lett 47. https://doi.org/10.1029/2019GL086611

Naveen, P.U., Sathapathy, S.K., Giri, Y., Singh, A.P., Radhakrishna, M., Rao, C.V., 2023. Crustal structure across the Central part of Narmada-Son Lineament, India based on the interpretation of aeromagnetic and gravity data: Geological implications. J Asian Earth Sci 255. https://doi.org/10.1016/j.jseaes.2023.105765

Olierook, H.K.H., Jiang, Q., Jourdan, F., Chiaradia, M., 2019. Greater Kerguelen large igneous province reveals no role for Kerguelen mantle plume in the continental breakup of eastern Gondwana. Earth Planet Sci Lett 511, 244–255. https://doi.org/10.1016/j.epsl.2019.01.037

Pang, F., Liao, J., Ballmer, M.D., Li, L., 2023. Plume-ridge interactions: Ridgeward versus plate-drag plume flow. Solid Earth 14, 353–368. https://doi.org/10.5194/se-14-353-2023

Patranabis-Deb, S., Saha, D., Santosh, M., 2020. Tracking India within precambrian supercontinent cycles, in: Springer Geology. Springer, pp. 105–143. https://doi.org/10.1007/978-3-030-15989-4_3

Petersen, S. V., Dutton, A., Lohmann, K.C., 2016. End-Cretaceous extinction in Antarctica linked to both Deccan volcanism and meteorite impact via climate change. Nat Commun 7, 1–9. https://doi.org/10.1038/ncomms12079

Prasad, K.N.D., Singh, A.P., Tiwari, V.M., 2018. 3D upper crustal density structure of the Deccan Syneclise, Central India. Geophys Prospect 66, 1625–1640. https://doi.org/10.1111/1365-2478.12675

Qureshy, M.N., 1982. Geophysical and Landsat lineament mapping — An approach illustrated from west-central and south India. Photogrammetria 37, 161–184.

Rai, S.S., Kumar, T.V., Jagadeesh, S., 2005. Seismic evidence for significant crustal thickening beneath Jabalpur earthquake, 21 May 1997, source region in Narmada-Son lineament, central India. Geophys Res Lett 32, 1–5. https://doi.org/10.1029/2005GL023580

Rao, K.M., Kumar, M.R., Rastogi, B.K., 2015. Crust beneath the northwestern Deccan Volcanic Province, India: Evidence for uplift and magmatic underplating. J Geophys Res Solid Earth 120, 3385–3405. https://doi.org/10.1002/2014JB011819

Ribe, N.M., 1996. The dynamics of plume-ridge interaction 2. Off-ridge plumes. J Geophys Res Solid Earth 101, 16195–16204. https://doi.org/10.1029/96jb01187

Ribe, N.M., Christensen, U.R., 1999. The dynamical origin of Hawaiian volcanism, Earth and Planetary Science Letters.

Ribe, N.M., Christensen, U.R., 1994. Three-dimensional modeling of plume-lithosphere interaction. J Geophys Res 99, 669–682. https://doi.org/10.1029/93JB02386

Richards, M.A., Alvarez, W., Self, S., Karlstrom, L., Renne, P.R., Manga, M., Sprain, C.J., Smit, J., Vanderkluysen, L., Gibson, S.A., 2015. Triggering of the largest Deccan eruptions by the Chicxulub impact. Bulletin of the Geological Society of America 127, 1507–1520. https://doi.org/10.1130/B31167.1

Richards, M.A., Duncan, R.A., Courtillot, V.E., 1989. Flood Basalts and Hotspot Tracks: Plume Heads and Tails. Science (1979) 246, 103–107.

Schoene, B., Eddy, M.P., Samperton, K.M., Keller, C.B., Keller, G., Adatte, T., Khadri, S.F.R., 2019. U-Pb constraints on pulsed eruption of the Deccan Traps across the end-Cretaceous mass extinction. Science (1979) 363, 862–866. https://doi.org/10.1126/science.aau2422

Schoene, B., Samperton, K.M., Eddy, M.P., Keller, G., Adatte, T., Bowring, S.A., Khadri, S.F.R., Gertsch, B., 2015. U-Pb geochronology of the Deccan Traps and relation to the end-Cretaceous mass extinction. Science (1979) 347, 182–184. https://doi.org/10.1126/science.aaa0118

Singh, A., Kumar, M.R., Kumar, N., Saikia, D., Solomon Raju, P., Srinagesh, D., Rao, N.P., Sarkar, D., 2012. Seismic signatures of an altered crust and a normal transition zone structure beneath the Godavari rift. Precambrian Res 220–221, 1–8. https://doi.org/10.1016/j.precamres.2012.07.006

Singh, A., Singh, C., Kennett, B.L.N., 2015. A review of crust and upper mantle structure beneath the Indian subcontinent. Tectonophysics. https://doi.org/10.1016/j.tecto.2015.01.007

Singh, A.P., 1998. 3-D Structure and geodynamic evolution of accreted igneous layer in the Narmada-Tapti region (India). J Geodyn 25, 129–141.

Sleep, N.H., 1997. Lateral flow and ponding of starting plume material. J Geophys Res Solid Earth 102, 10001–10012. https://doi.org/10.1029/97jb00551

Sprain, C.J., Renne, P.R., Clemens, W.A., Wilson, G.P., 2018. Calibration of chron C29r: New high-precision geochronologic and paleomagnetic constraints from the Hell Creek region, Montana. Bulletin of the Geological Society of America 130, 1615–1644. https://doi.org/10.1130/B31890.1

Torsvik, T.H., Cocks, L.R.M., 2013. Gondwana from top to base in space and time. Gondwana Research. https://doi.org/10.1016/j.gr.2013.06.012

Unrug, R., 1996. The assembly of Gondwanaland. Episodes 19, 11–20.

White, R.S., McKenzie, D., 1995. Mantle plumes and flood basalts. J Geophys Res 100. https://doi.org/10.1029/95jb01585

Whittaker, J.M., Afonso, J.C., Masterton, S., Müller, R.D., Wessel, P., Williams, S.E., Seton, M., 2015. Long-term interaction between mid-ocean ridges and mantle plumes. Nat Geosci 8, 479–483. https://doi.org/10.1038/NGEO2437

Zhao, D., 2015. The 2011 Tohoku earthquake (Mw 9.0) sequence and subduction dynamics in Western Pacific and East Asia. J Asian Earth Sci 98, 26–49. https://doi.org/10.1016/j.jseaes.2014.10.022

Figure captions:

Figure 1 a) Geological setting of the Indian subcontinent showing major geological provinces, which constitute the Indian Peninsular craton and the continental-scale rift structures. DVP: Deccan volcanic province, DAFB: Delhi-Aravalli fold belt, BKC: Bundelkhand craton, VB: Vindyan basin, NSL: Narmada-Son lineament, CR: Cambay rift, CGGC: Chotanagpur Gneissic complex, NSFB: North Singhbhum fold belt, SC: Singbhum craton MR: Mahanadi Rift, CTB Chattisgarh Basin, BC: Bastar craton, KGR: Krishna Godavari Rift, EDC: Eastern Dharwar craton, WDC: Western Dharwar Craton, CG: Closepet Granite, CB: Cuddapah basin, SGT: Southern Granulite terrain. b) A diagrammatic presentation of the activities of the NSL, KGR, MR, Kergueran, and Réunion plume throughout geological history.

Figure 2 a. i) Numerical model simulation of an ascending plume influenced by a pre-existing rift in the lithosphere for a small plume-rift distance (150 Km). Note that the rift induces an asymmetric spreading of the plume head and accumulation of plume materials beneath the rift axis (a detailed description is provided in the text). Green arrows in the magnified panel show the velocity field in the mantle. Calculated plots of b) deflection of Moho and the surface topography varying with horizontal distance at different time instances (indicated in the colours in the insets), and c) variations of the Buoyancy flux at two locations (AA′ and BB′) on either side of the plume axis shown in the inset in panel a. d) Depth wise profiles of horizontal velocity component (V_x) at AA′ and BB′.

Figure 3 a. i) Plume simulation in numerical models with a plume-rift distance of 200 km. It is to be noted that the setting shows relative weak plume-rift interactions (on the right side), resulting in a more symmetrical plume underplating structure beneath the lithosphere and strong LAB erosions on either flank of the plume-head. The plume experiences rift-ward deflection implying an influence of the pre-existing rift. Detail underplating patterns (a. ii) and downward lithospheric drag (a. iii) are highlighted in the enlarged views of the overlying panels. b) Fluctuations of Moho and surface topography in the horizontal direction in different time transects from model simulations. c) Variation of buoyancy fluxes in two locations of the plume-head on either side of the plume axis show at different time. d) Depth-wise profiles of horizontal velocity component (V_x) at AA′ (d.i) and BB′ (d.ii).

Figure 4 a. i) Evolution of a plume in models with large plume-rift distance (250 km), showing maximum Moho downwrapping, and plume tilting opposite to the rift axis. It is to be noted that the plume materials are accumulated beneath the newly formed rift (a. ii) due to higher rift induced divergent velocity, whereas the pre-existing rift fails to reactivate (a. iii). b) The changes in Moho depth and surface topography along the horizontal direction are presented at different time intervals. c) Temporal variations in the buoyancy fluxes at two distinct locations of the plume head (A″ and B″), on either side of the plume axis. d) Depth profiles of the horizontal velocity component (V_x) at locations AA′ (d.i) and BB′ (d.ii).

Figure 5. Model calculated plots of the plume-related physical quantities. a) Variations of the volume ratio of plume material between right- and left-branch of plume-head as a function of plume-rift distance (δ) in different plate velocity (V_p). b) Calculated plots of strain rate varying with time (in Ma) for increasing δ and V_p. c) Changes of plume-head buoyancy with δ at varying V_p. d) Variations of the ratio between horizontal velocities measured at LAB depth and the plate surface.

Figure 6 Fields of interacting and non-interacting plume-paleo rifts in a space defined by plume-rift distance (*x*-axis) and plate velocity (*y*-axis). Increasing plate velocity or decreasing plume-rift distance facilitates the development of an interacting plume-rift system, which favours rift-ward plume flows.

Figure 7 a) A geological map of the Narmada son rift system displaying its major lineament pattern. b) Horizontal variations of Moho depth and heat flows along the section AA′ in panel b. Note that Moho downwrapping and high heat-flow regime localize at the same place above the rift. c) Model simulation showing the location of partial melting beneath the pre-existing rift. Abbreviations used are SNNF: Son-Narmada North Fault, SNSF: Son-Narmada South Fault, TS: Tan Shear, CIS: Central Indian Shear. SNF: Son–Narmada Fault; TNF: Tapti North Fault; BSF; Barwani Sukta Fault; PF: Purna Fault; KF: Kaddam Fault.

Figure 8 a) A geological map of the Krishna-Godavari rift system. b) Systematic variation of the Moho depth and corresponding heat flow along the section BB′ c) Model simulation showing underplating of the plume materials beneath the lithosphere, coupled with a selectively strong drag of the mantle lithosphere. It is to be noted that Moho downwrapping and high heat flow occur preferentially at the age of the underplated plume material. Abbreviations used are DVP: Deccan Volcanic Province; EDC: Eastern Dharwar Craton; GR: Godavari rift; EGMB: Eastren Ghat Mobile Belt; KF: Kaddam Fault; KGF: Kinnerasani-Godavari Fault; KLF: Kolleru-Lake Fault; GVF: Godavari Valley Fault.

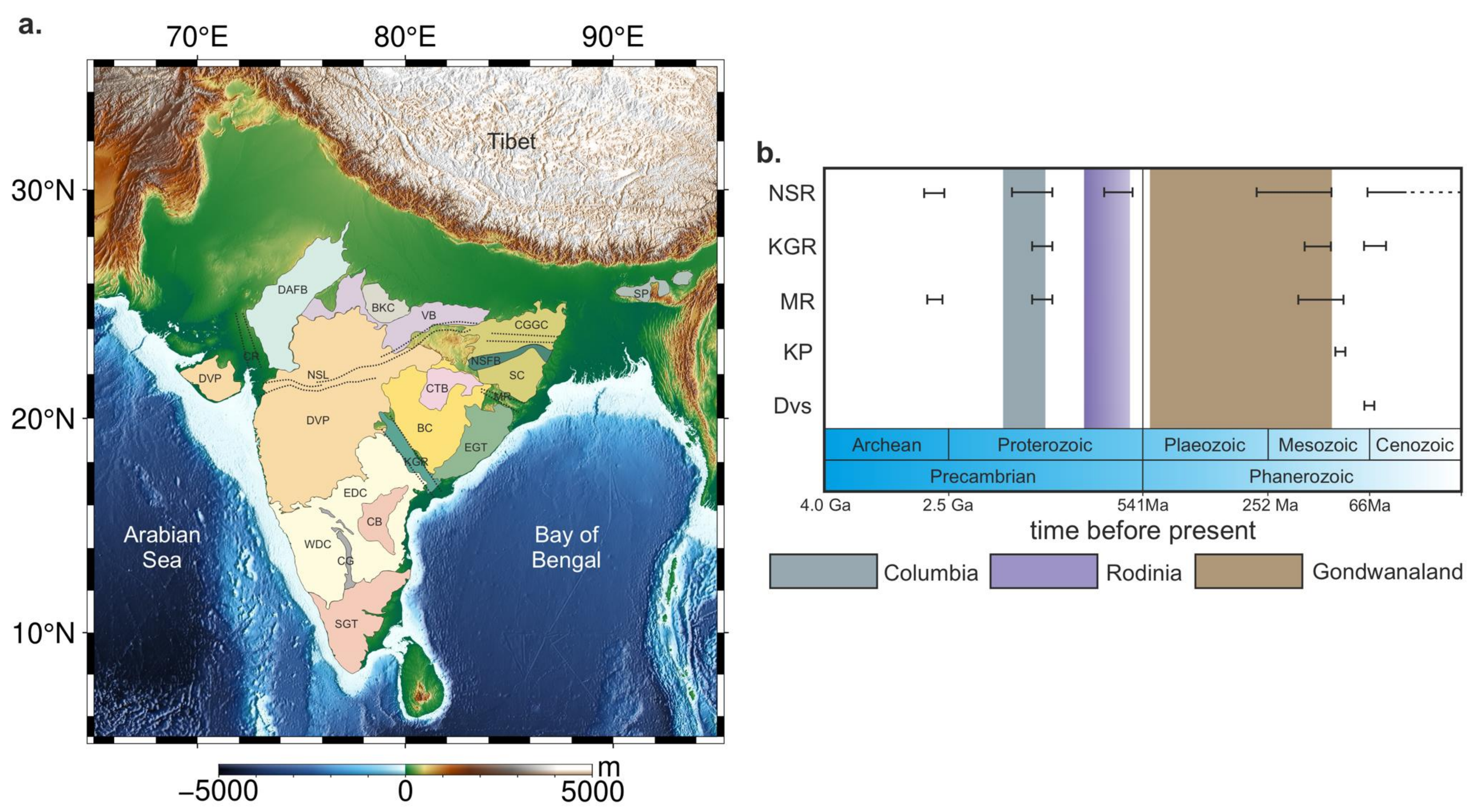

a.
70°E
80°E
90°E
30°N
20°N
10°N
Tibet
DAFB
BKC
VB
CGGC
NSFB
SC
SP
CR
DVP
NSL
CTB
MR
DVP
BC
EGT
KGR
EDC
CB
WDC
CG
SGT
Arabian Sea
Bay of Bengal
–5000
0
5000
m
b.
NSR
KGR
MR
KP
Dvs
Archean
Proterozoic
Plaeozoic
Mesozoic
Cenozoic
Precambrian
Phanerozoic
4.0 Ga
2.5 Ga
541Ma
252 Ma
66Ma
time before present
Columbia
Rodinia
Gondwanaland

Figure 1

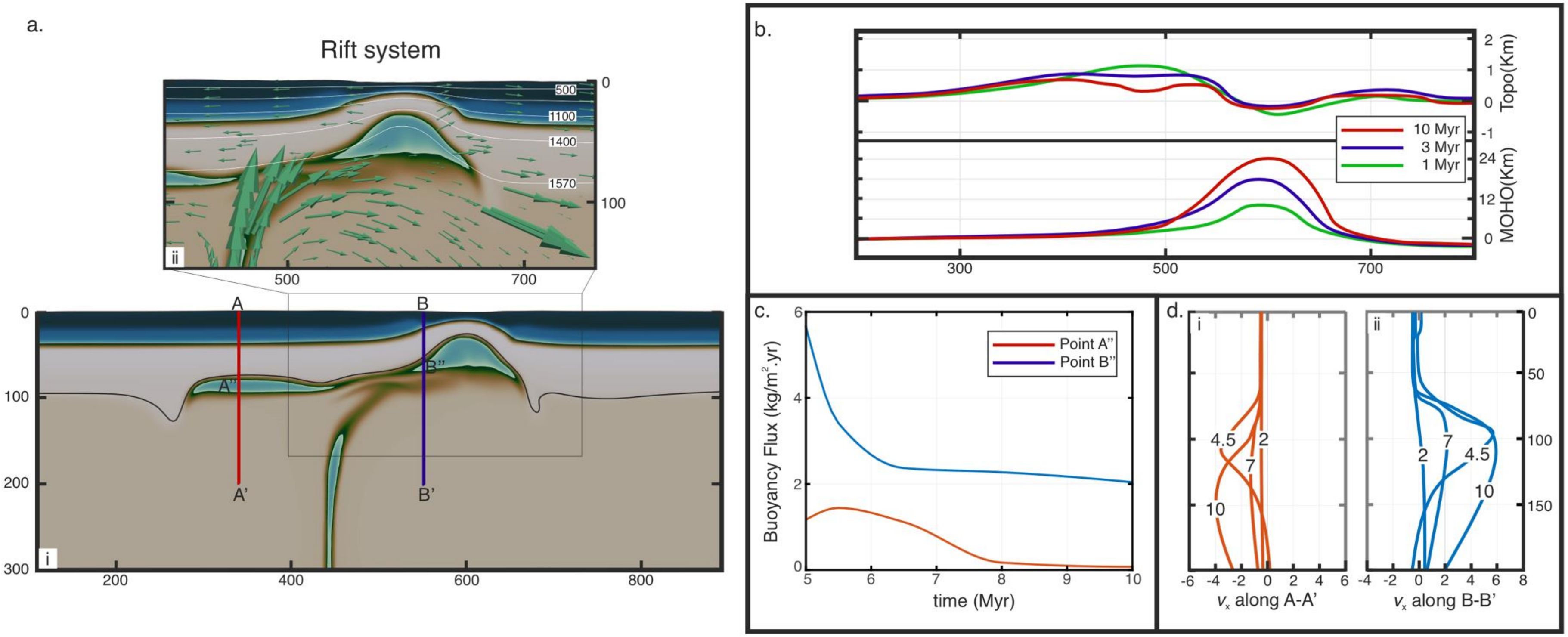
a.
Rift system
500
1100
1400
1570
ii
i
A
B
A''
B''
A'
B'
b.
Topo(Km)
MOHO(Km)
10 Myr
3 Myr
1 Myr
c.
Buoyancy Flux (kg/m².yr)
time (Myr)
Point A''
Point B''
d.
v_x along A-A'
v_x along B-B'

Figure 2

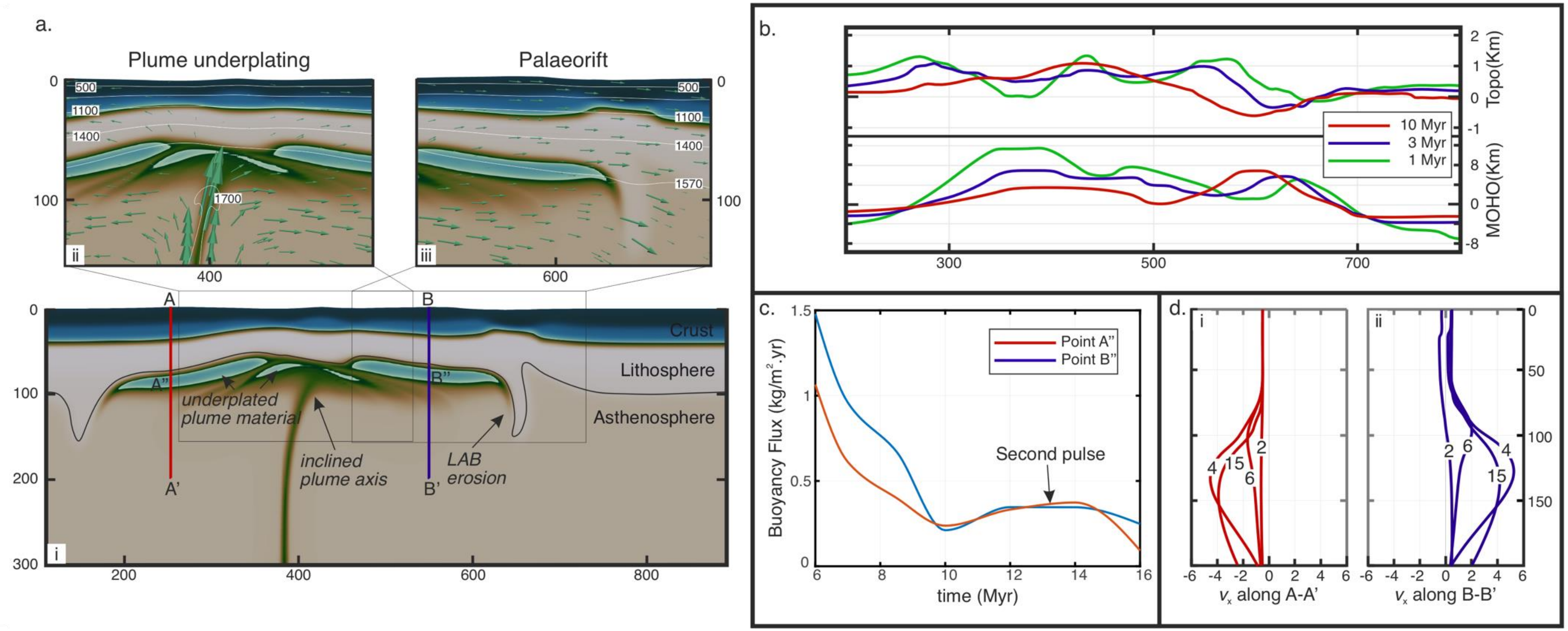

a.
Plume underplating
Palaeorift
500
1100
1400
1700
1570
Crust
Lithosphere
Asthenosphere
underplated plume material
inclined plume axis
LAB erosion
b.
Topo(Km)
MOHO(Km)
10 Myr
3 Myr
1 Myr
c.
Buoyancy Flux (kg/m².yr)
time (Myr)
Point A''
Point B''
Second pulse
d.
vx along A-A'
vx along B-B'

Figure 3

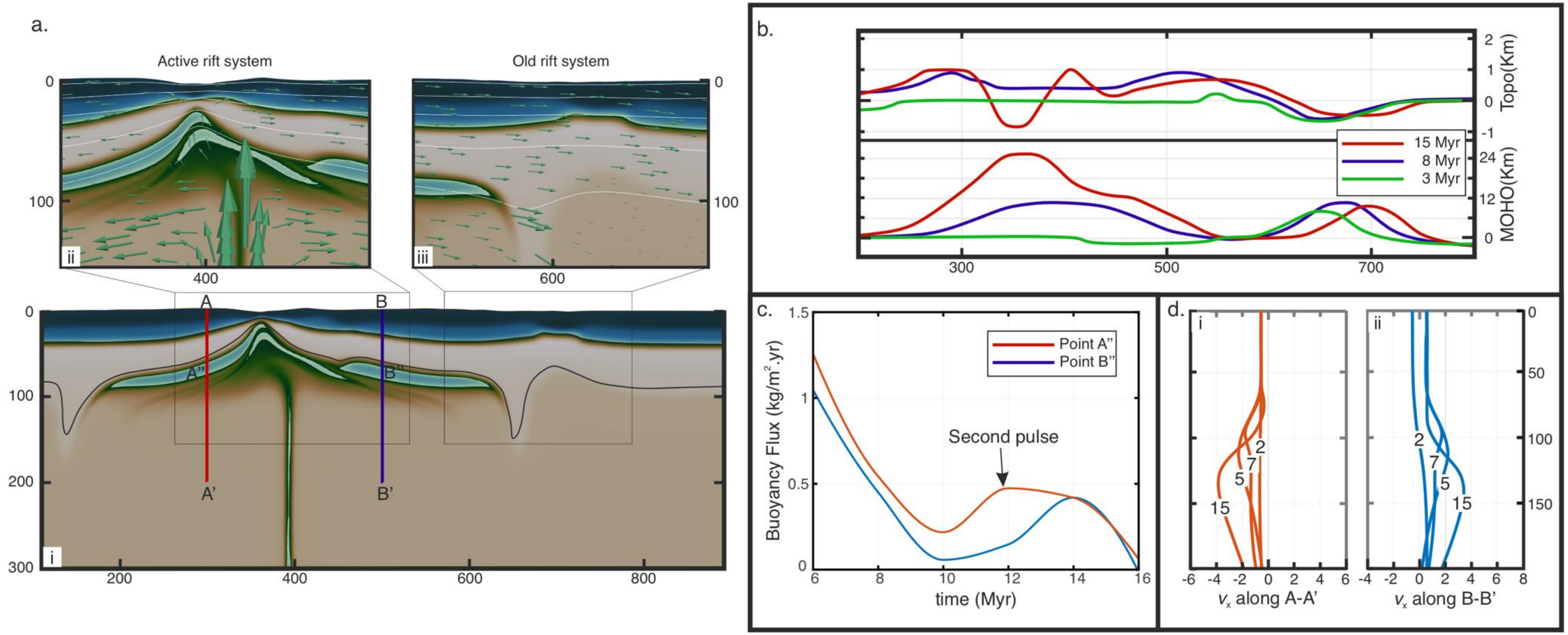

a.
Active rift system
Old rift system
A
B
A''
B''
A'
B'
b.
Topo(Km)
MOHO(Km)
15 Myr
8 Myr
3 Myr
c.
Buoyancy Flux (kg/m².yr)
time (Myr)
Point A''
Point B''
Second pulse
d.
v_x along A-A'
v_x along B-B'

Figure 4

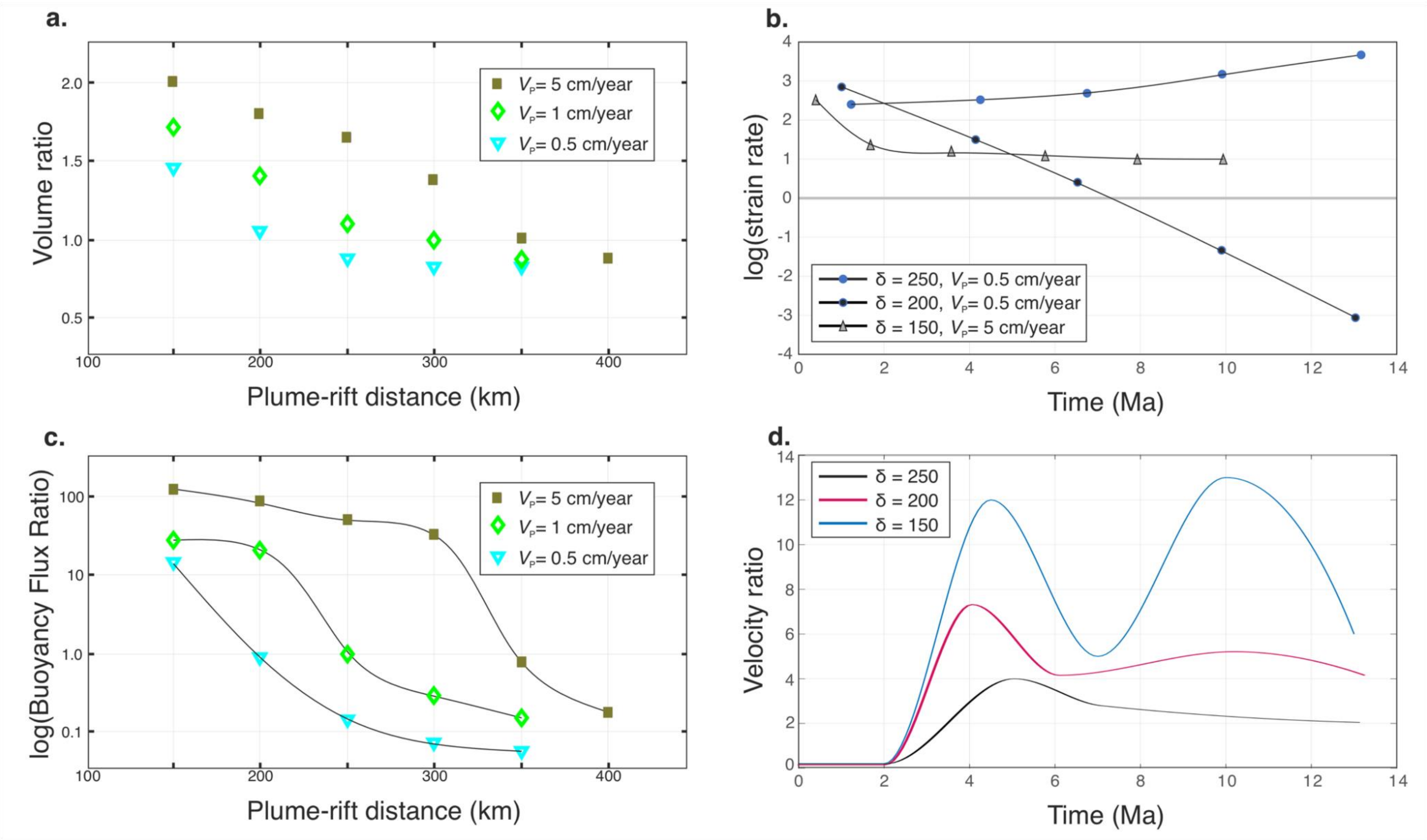

a.
Volume ratio
2.0
1.5
1.0
0.5
100
200
300
400
Plume-rift distance (km)
V_P= 5 cm/year
V_P= 1 cm/year
V_P= 0.5 cm/year
b.
log(strain rate)
4
3
2
1
0
-1
-2
-3
-4
0
2
4
6
8
10
12
14
Time (Ma)
δ = 250, V_P= 0.5 cm/year
δ = 200, V_P= 0.5 cm/year
δ = 150, V_P= 5 cm/year
c.
log(Buoyancy Flux Ratio)
100
10
1.0
0.1
100
200
300
400
Plume-rift distance (km)
V_P= 5 cm/year
V_P= 1 cm/year
V_P= 0.5 cm/year
d.
Velocity ratio
14
12
10
8
6
4
2
0
0
2
4
6
8
10
12
14
Time (Ma)
δ = 250
δ = 200
δ = 150

Figure 5

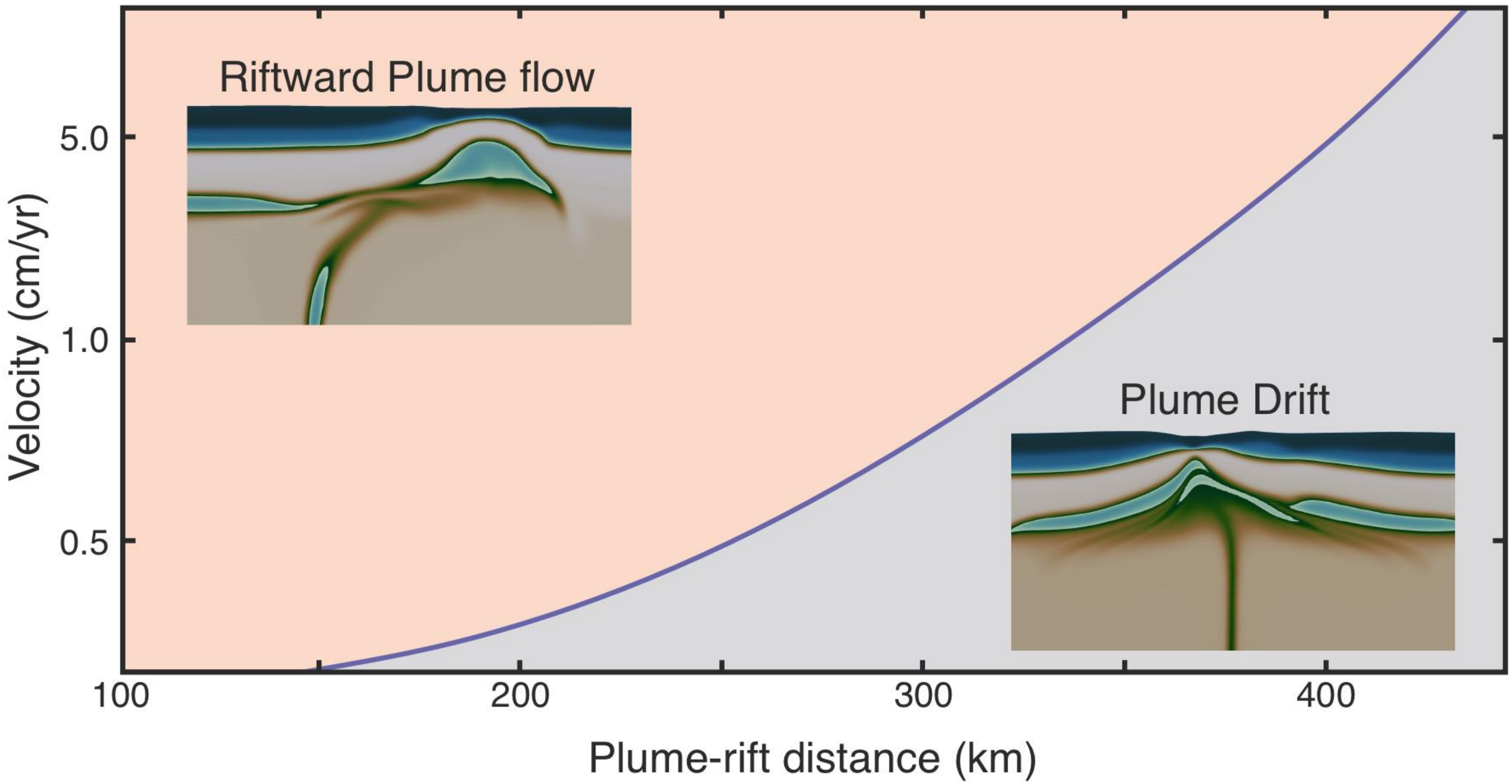

Riftward Plume flow
Plume Drift
5.0
1.0
0.5
Velocity (cm/yr)
100
200
300
400
Plume-rift distance (km)

Figure 6

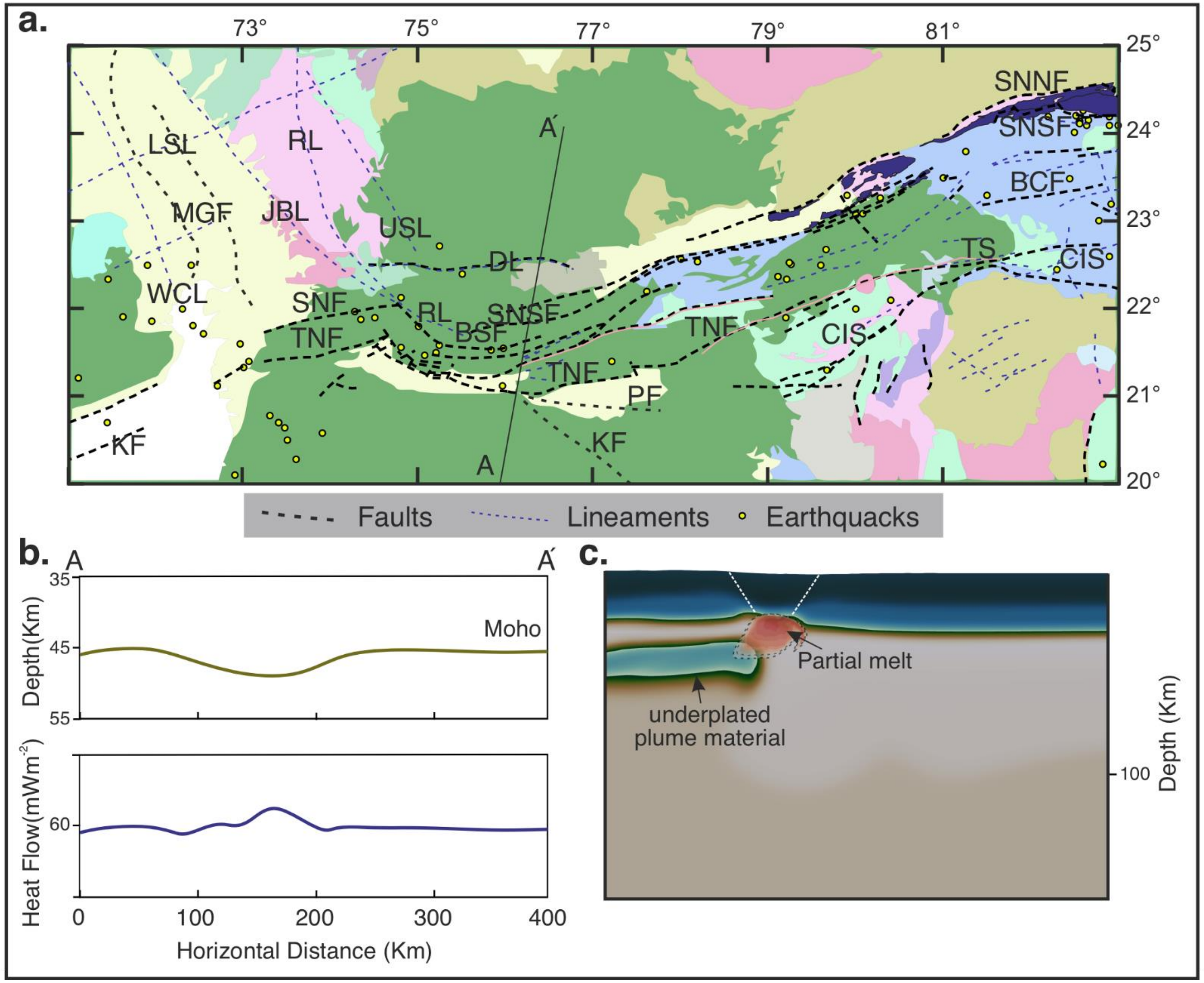
a.
73°
75°
77°
79°
81°
25°
24°
23°
22°
21°
20°
SNNF
SNSF
BCF
TS
CIS
LSL
RL
MGF
JBL
USL
DL
WCL
SNF
RL
SNSF
BSF
TNF
TNF
TNF
CIS
PF
KF
KF
A
Á
Faults
Lineaments
Earthquacks
b.
A
Á
Depth(Km)
35
45
55
Moho
Heat Flow(mWm^{-2})
60
0
100
200
300
400
Horizontal Distance (Km)
c.
Partial melt
underplated
plume material
100
Depth (Km)

Figure 7

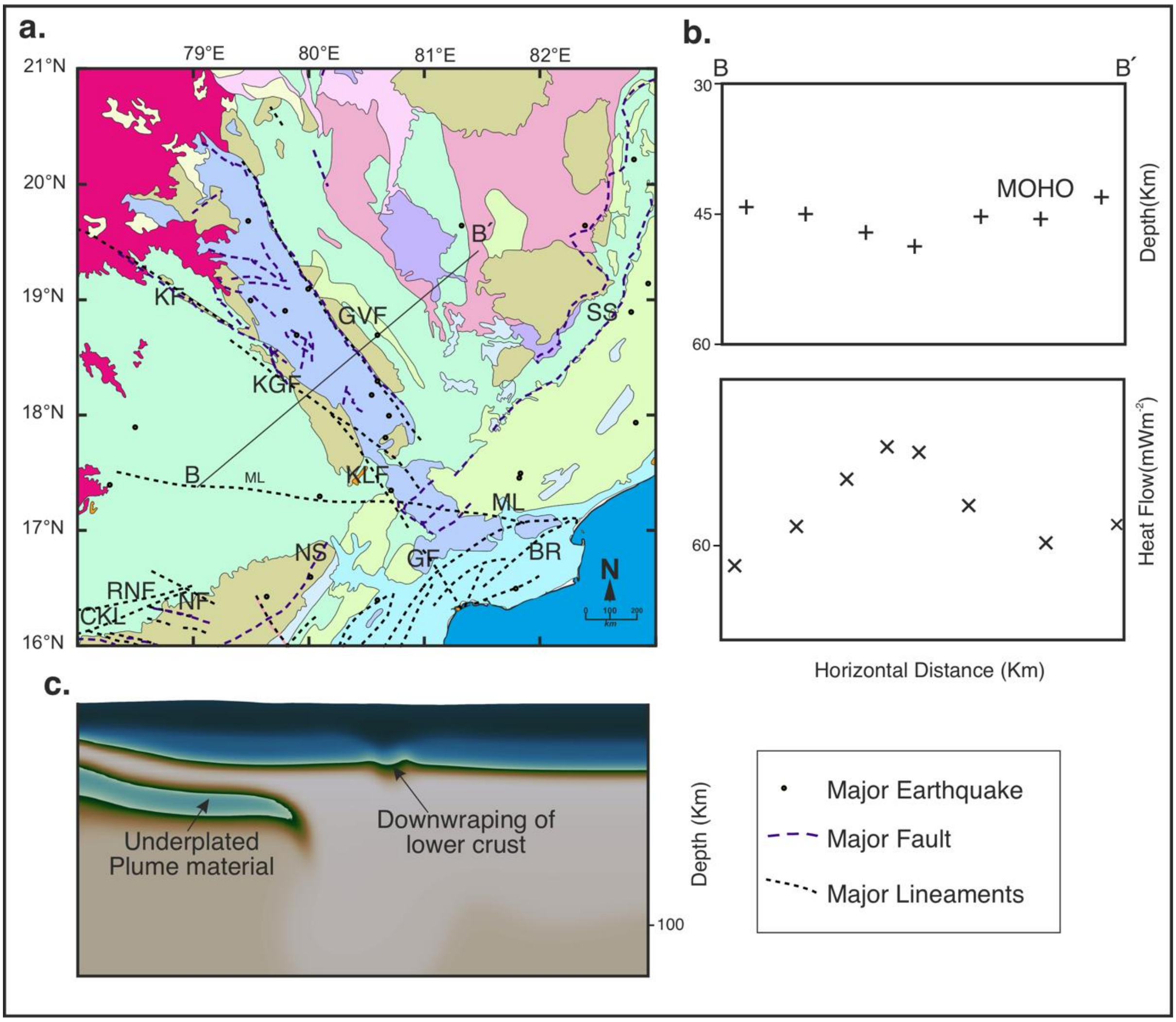
a.
b.
c.
21°N
20°N
19°N
18°N
17°N
16°N
79°E
80°E
81°E
82°E
KF
GVF
KGF
B
ML
KLF
B´
SS
ML
NS
GF
BR
RNF
NF
CKL
N
B
B´
MOHO
Depth(Km)
30
45
60
60
Heat Flow(mWm⁻²)
Horizontal Distance (Km)
Underplated
Plume material
Downwraping of
lower crust
Depth (Km)
100
Major Earthquake
Major Fault
Major Lineaments

Figure 8

Table 1. Model parameters used in numerical simulations

Parameters	Values
Model length(L)	1000km
Model height(H)	410km
Thickness- upper crust(t_{uc})	25km
lower crust(t_{lc})	15km
lithospheric mantle(t_{lm})	40-80km
Plume diameter	20-100km
Plate velocity	0.25-5cm/year
Plume-rift distance	0-300km
Surface Temperature (Ts1)	293 K
Temperature at upper crustal base (Ts2)	681 K
Temperature at lower crustal base (Ts3)	823 K
Temperature at the base of the lithosphere (Ts4)	1573 K
Model base temperature (Tb)	1700 K
Initial plume temperature (Tp)	1700-1900 K
Heat production at upper crust (A)	1.5e-6 W/m^3
Thermal conductivity- upper crust (k1)	2.5 W/m.K
lower crust (k2)	2.5 W/m.K
lithospheric mantle (k3)	3.5 W/m.K
Layer surface heat flow- upper crust (qs1)	0.065357 W/m^2
lower crust (qs2)	0.035357 W/m^2
lithospheric mantle (qs3)	0.035357 W/m^2

Table 2. Parameters for calculating material model

	Upper crust	Lower crust	Lithospheric mantle	Upper mantle	Plume	Seed	Sticky air
Density *(kg m-3)*	2750	2900	3325	3300	3275	3325	1
Grain size *(m)*			1e-3				
Thermal expansivities			2e-5				
Heat capacities			750				
Prefactors for dl *(MPa^{-n} s^{-1})*	1.1e-28	1.0e-21	2.41e-16	5.5e-16	5.5e-16	1.1e-28	1e-19
Stress exponents for dl	4.0	3.0	3.5	3	3	4.0	1
Activation energies for dl *(J mol^{-1})*	223.e3	356.e3	540.e3	540.e3	540.e3	223.e3	0
Activation volumes for dl *(J Pa^{-1})*	0	0	0	14e-6	14e-6	0	0
Prefactors for df *(MPa^{-n} s^{-1})*	1.1e-11	1e-11	2.41e-11	5.41e-11	5.41e-11	1.1e-11	1.92e-11
Grain size exponents for df	0	0	2.5	2.5	2.5	0	0
Activation energies for df *(J mol^{-1})*	223.e3	356.e3	540.e3	540.e3	540.e3	223.e3	335e3
Activation volumes for df *(J Pa^{-1})*	0	0	0	14e-6	14e-6	0	4e-6